Surface & Grain Boundaries Co-passivation by Fluorocarbon based Bifunctional Molecules for Perovskite Solar Cells with Efficiency Over 21%

Pengfei Guo, Qian Ye, Xiaokun Yang, Jin Zhang, Fei Xu, Dmitry Shchukin, Bingqing Wei, Hongqiang Wang**

Mr. P. Guo, Dr. Q. Ye, Mr. X. Yang, Ms. J. Zhang, Dr. F. Xu, Prof. B. Wei, Prof. H. Wang
State Key Laboratory of Solidification Processing, Center for Nano Energy Materials, School of Materials Science and Engineering, Northwestern Polytechnical University and Shaanxi Joint Laboratory of Graphene (NPU), Xi'an, 710072, P. R. China
Dr. Q. Ye
Research & Development Institute of Northwestern Polytechnical University in Shenzhen, Northwestern Polytechnical University, Xi'an, 710072, P. R. China
Prof. D. Shchukin,
Stephenson Institute for Renewable Energy, Department of Chemistry, University of Liverpool, Crown Street, Liverpool, L69 7ZD, United Kingdom
Prof. B. Wei
Department of Mechanical Engineering, University of Delaware, Newark, Delaware 19716, United States
Email: yeqian213@nwpu.edu.cn; hongqiang.wang@nwpu.edu.cn

Key words: perovskite solar cell, surface passivation, grain boundaries passivation, photo-conversion efficiency, moisture durability

Abstract:

The low-temperature processing in perovskite films always results in the formation of submicrometer scale grains and consequent abundant defects that lead to carriers recombination, hysteresis as well as moisture degradation. Passivation of defects at either surface or grain boundaries (GBs) thus promises great advances for developing high performance perovskite solar cells (PSCs). By taking the co-passivation agent of 1H, 1H-Perfluorooctylamine (PFA) as the example, we present in this work a simple and effective surface & GBs co-passivation strategy based on bifunctional molecules with fluorocarbon chains to achieve PSCs with highly improved photo-conversion efficiency (PCE) and stability. It was demonstrated that such co-passivation strategy leads to 53.3% PCE enhancement in the $MAPbI_3$ PSCs, as well as achampion PCE of 21.31% in CsFAMA type PSCs, and remarkable stability with 3% PCE loss after 2500 hrs of storage in the humidity of 70 ± 5% at room temperature. Our result thus shows great potentials of surface & GBs co-passivation by fluorocarbon based molecules for accessing high performance PSCs based on protocols of defects manipulation.

Solution-processed lead halide perovskite solar cells (PSCs) have emerged as one of the most intensive research areas in photovoltaic fields[1], owing to their achieved remarkable power conversion efficiencies (PCEs) of 23.3%[2] that could challenge the established crystalline silicon and thin film solar cells. Within the notable advantages of PSCs, the facile low-temperature synthesis determines critically the potentials for the low-cost commercialization. This, however, would introduce abundant defects existing at either surface or grain boundaries (GBs) within the active layer, which incur trap-assisted non-radiative recombination as well as the initialization of the perovskite degradation by the permeated moisture or oxygen[3]. In this regard, defects passivation is highly desirable not only for further boosting the PCE to a new height but also for prolonging the durability of the PSCs. Surface passivation via coating molecules containing passivation groups, such as amino/ammonium[4], pyridine[5], and carboxyl[6], on the surface of the preformed perovskite layer, has been a direct route and showed preliminary success on the efficiency and durability enhancement. A notable example is that benzylamine modification resulted in improved PCEs from 14.2% to 17.3% and prolonged moisture-durability over 2900 hrs[4a].

While considering the larger specific surface areas of GBs that act as centers for non-radiative recombination[3a,7a-7h] than that of the perovskite layer surface, more performance enhancement is anticipated if strategies are developed for GBs passivation. However, there has been a debate that GBs are inert toward charge recombination[7i] and might even be beneficial for charge separation[7j]. Recently, Jodlowski et al.[8] demonstrated that adding the guanidinium cation into the perovskite precursors that might lead to the defects passivation of GBs, gave rise to a high PCE of 20.15%. Similarly, the recently developed GBs passivation by adding the passivation agents into the precursors[7h,8,9], post-treating the as-prepared perovskite films via passivation agents,[10] and introducing the passivation agent via anti-solvent,[11] leads to pronounced performance improvement. However, rare of them has taken the contribution of surface passivation into consideration, and it remains obscure in these

studies if GBs passivation plays a vital role for PCE enhancement. More recently, Liu group addressed the importance of GBs passivation by using semiconducting passivation molecules that could result in the PCE enhancement up to 19.3%,[12] while they found that surface passivation had almost negligible contribution. So far, defects passivation of perovskite films at either surface or GBs separately has been proven successful for the enhancement of the PSCs efficiency and stability. It would be highly promising if a strategy can be developed by taking the advantages of both surface and GBs passivations.

In the present study, by taking the co-passivation agent of 1H, 1H-Perfluorooctylamine (PFA) as the example, we demonstrate a surface and GBs co-passivation strategy by the fluocarbon based bifunctional molecules, which was found to be much effective to decrease the defect densities and inhibit the non-radiative recombination. By using the surface & GBs co-passivation strategy, a remarkable 53.3% enhancement in PCE was achieved within the archetypal $MAPbI_3$-based PSCs. Meanwhile, the cells demonstrated much improved moisture-durability owing to the hydrophobic fluorocarbon chain. We further applied such co-passivation strategy on the mixed-cation lead mixed halide PSC, and achieved encouraging stable PSCs with the champion efficiency of 21.31%, which is among the top in the records of defects passivation related performance of PSCs.[7h,8,9a-9c,9e,9g-9h,10-13]

Owing to the strong binding energy of the amino group in PFA (**Figure 1a**) with perovskite (calculated binding energy of 51.88 kJ/mol[14]), PFA is anticipated to be able to passivate the uncoordinated lead at both of the surface and GBs, as depicted in **Figure 1b** Experimentally, we intended to introduce the CF_3 based molecules to different locations of a perovskite layer through the following routes: i) incorporating via anti-solvent of chlorobenzene, and ii) spin-coating on the preformed perovskite film, which is expected to result in respectively surface & GBs passivation and surface-only passivation (see Routes A and C in **Scheme S1**). All the devices in present work adopt the planar heterojunction configuration of FTO/TiO_2/perovskite/spiro-OMeTAD/Au, and the formation process of

perovskite and configuration of the perovskite device are shown in supporting information. Similar to the previous reports[14], we failed in producing the uniform film (**Figure S1 and Figure S2a**) based on introducing passivation agent via precursors (Route B in Scheme S1) owing possibly to the hydrophobic nature of PFA. We therefore adopted Routes A and C in present study as experimentally they do not influence the formation of the homogeneous films with full surface coverage over the entire substrate (**Figure S1**). The produced films via Route A and C are denoted as $MAPbI_3$-PFA and $MAPbI_3$/PFA respectively. For each route, PFA with different concentrations (0.6, 1.2, 2.4, 6.0 and 15 mg/mL), denoted by PFA-1, PFA-2, PFA-3, PFA-4 and PFA-5, respectively, was used to explore the optimized passivation effects.

Figures 1c and 1d depicts the surface morphologies of the prepared $MAPbI_3$/PFA and $MAPbI_3$-PFA films, respectively. Different from the case that incorporating polymers into the perovskite layer via anti-solvent alters the perovskite crystal formation,[11] introducing of a low concentration of PFA in our study has little influence on the morphological change comparing to the control film (without PFA), and there is also no significant grain-size alteration after PFA modifications (as seen in **Figures 1c-d, S2b and S3a-d**). The cross-section SEM observations (**Figures S3g-i**) indicate that the $MAPbI_3$-PFA film has more uniform and dense surface, fewer voids, and smaller grain protrusions than those of $MAPbI_3$/PFA and control films. The surface profiles of the films with different passivation ways revealed in AFM observations (**Figures 1e-1f, S4**) demonstrate obviously different surface root-mean-square roughness: 11.0 nm for the $MAPbI_3$-PFA film, 26.8 nm for the $MAPbI_3$/PFA film and 27.2 nm for the control film. It is therefore clear that the strategy of co-passivation favors more for the formation of perovskite film with better qualities than that of the control film. The improved film quality might be because the introduced passivant suppress overcrystallization of PbI_2, which is usually associated with nonuniform film coverage and pinhole formation.[12] Further X-ray photoelectron spectroscopy (XPS) analysis (**Figure 1g**) revealed the evident peak of F_{1s} located at around 685.7 eV for both $MAPbI_3$-

PFA and $MAPbI_3$/PFA films, illustrating the existence of PFA molecules on the surface of the both films. However, signals of F_{1s} were not detected for both films (**Figure S5**) indepth of the film, which might be due to the removing of light elements by the high energy Ar ion beam during the XPS depth profile characterization.

To further explore if F element is involved deeply in the perovskite layer for the $MAPbI_3$-PFA film, we employed the energy dispersive X-ray spectroscopy in the cross section SEM (SEM-EDS) observations. **Figure 1h** shows the cross-section SEM image that depicts the six layers in the device. The SEM-EDS observation (see more details in **Figure S6**) revealed the distribution of F elements throughout the perovskite layer (indicated by the Pb element distribution) and the FTO layer (indicated by the Sn element distribution). An initial conclusion can thus be drawn that PFA is indeed deeply involved in the perovskite layer for the $MAPbI_3$-PFA film. Comparatively, F element was not detected in the perovskite layer by similar SEM-EDS observation (**Figure S6a**), which may be because such nanoscale thickness of F distribution on the surface is out of the resolution detection of the EDS analysis. Therefore, these results clearly demonstrate that F element does not exist in perovskite in case of surface-only passivaition while F element exist throughout the perovskite layer in case of surface& GBs co-passivaition. By using the EDS in Transmission Electron Microscopy cross section characterization, we further intended but failed to verify if the F element distribute only in the GBs locations of the perovskite layer, owing to the easy damage of the layers structure[15] during the sample preparation (see **Figure S7**). Finally we have to exclude the existing of PFA in the perovskite lattice via X-ray diffraction (XRD) analysis, which is shown in **Figure 1i** and **Figure S8**. All the XRD patterns of perovskite films with or without PFA modification showed strong diffraction peaks of $MAPbI_3$ located at approximately 14.15° and 28.5° (2θ) with no clear presence of a secondary phase. This indicates introducing the passivation molecules in present study does not influence the perovskite crystallinity, which is in agreement with the previous reports.[16] Above characterizations indicate that the

passivation molecule decorates surface and GBs throughout the depth of the films, which is similar with a recent work reported by Liu Group.[12] Comparatively, route C of surface coating can only bring PFA to the surface of the perovskite layer as evidenced by XPS analysis above and SEM-EDS characterization (**Figure S6**). Therefore, the expectation of surface & GBs co-passivation in $MAPbI_3$-PFA film and surface-only passivation in the $MAPbI_3$/PFA film shown in **Scheme S1** can be respectively confirmed. It is thus of great interest to further explore their impacts on the PSCs performance.

The photovoltaic properties of PSCs were characterized systematically and the results were summarized in **Figure S9** and **Tables S1-S2**. It was found that the PFA concentrations play important roles in the performance of PSCs, and the champion efficiency locates at the concentration of PFA-4 for both type devices (**Figure S9**). **Figure 2a** shows the current density-voltage (*J-V*) curves (measured under simulated AM1.5 illumination of 100 mW cm^{-2}) of the champion devices via different passivation methods. The scan rate for all the *J-V* curves in present study is 0.2 V/s. The champion efficiency of the co-passivation device reached 16.18%, while the device via the surface-only passivation reached 14.48%, and the device without passivation (control device) reached 12.71%. As shown in **Figure 2a**, comparing to the obvious hysteresis in the control device and less-visible hysteresis in the surface-only passivated device, the co-passivated device demonstrated much more reduced and virtually negligible hysteresis. This result indicates GBs passivation is important to help reduce/eliminate the hysteresis in PSCs. To take an overview of the passivation effects on PSCs performance, the histograms of more than 48 solar cells with different passivation strategies are shown in **Figure 2b**. It can be seen that the devices via the surface-only passivation and co-passivation exhibited narrower PCE distributions than those of the control devices, indicating the improved reproducibility by the passivation strategies. The corresponding external quantum efficiency (EQE) spectra of cell devices depicted in **Figure 2c** indicate that co-passivation results in an increase over the entire visible-light range and

broad plateaus with a maximum value over 90%, reflecting a high charge-collection efficiency of the PSCs. The calculated integrated short-circuit current density (J_{sc}) values are 20.09, 20.39 and 21.63 mA/cm^2 for devices of control, surface-only passivation, and co-passivation, respectively, which match well with the values obtained from the *J-V* curves in **Figure 2a**. It should be noted that the average efficiencies of the devices (**Figure 2b**) illustrate an obvious PCEs increase of 53.3% for device via the co-passivation (from 10.12% to 15.51%), which is much higher than the increase of the devices via the surface-only passivation (25.7% increase, from 10.12 to 12.72%) and other similar works.[7h,8,9a-9c,9e,9g-9h,10-13]

Further work is undertaken to clarify why the co-passivation leads to much higher PSCs performance. It was found that the surface-only passivation had little effects on the UV-vis absorption of the resulted films (**Figure S10a**), while the co-passivated film showed improved UV-Vis absorption performance owing possibly to the improved film quality as described above (**Figure S10b**), which is in agreement with the EQE results (**Figure 2c**). In addition, the co-passivation was shown to be able to decrease the charge transfer resistance (see **Figure S11**), indicating the more efficiency of hole extraction as well as the higher Fill factor (FF), which is in line with the previous report.[17] The steady-state photoluminescence (PL) of the perovskite films deposited on TiO_2/FTO substrates shown in **Figure 2d** and **Figure S12a** revealed the PL intensity gradually increases as the concentrations of PFA increasing in the $MAPbI_3$ film. But the intensity for the surface-only passivated film is lower than that of the co-passivated film (**Figure 2d** indicating the less passivation effect of the surface-only modification. Interestingly, the PL intensity of the $MAPbI_3$-PFA-5 device is higher than that of $MAPbI_3$-PFA-4 but the PCE is lower, which can be further explained by a clear PL quenching for the $MAPbI_3$-PFA-4/Spiro-OMeTAD film but not for the $MAPbI_3$-PFA-5/Spiro-OMeTAD (See **Figure S12b**), owing possibly to the formation of the too-thick PFA layer that blocks the holes transport.

The carrier dynamics of the perovskite films were investigated to gain more insight into the mechanism of the increased PSCs performance. The time-resolved photoluminescence (TRPL) measurements shown in **Figure 2e**, revealed a much faster PL decay for the control than of the PFA-treated films. The PL decay curves were fitted to the following bi-exponential rate law:

$$Y=A_1\exp(-t/\tau_1)+ A_2\exp(-t/\tau_2)+y_0 \quad (1)$$

where A_1 and A_2 are the relative amplitudes, τ_1 and τ_2 is the lifetime for the fast and slow decay, respectively, and the PL lifetime is considered as the average of fast and slow lifetimes.[18] The fast decay is related to trap-assisted recombination at defects, whereas the slow decay is related to radiative recombination inside the grains. As shown in **Table S3**, the co-passivated film exhibits average lifetime of τ_{avg}=95.85 ns with τ_1=23.7 ns and τ_2=121.2 ns. In contrast, the surface-only passivated film gives τ_{avg}=72.98 ns with τ_1=18.3 ns and τ_2=102.7 ns, and the control film τ_{avg}=9.75 ns with τ_1=2.9 ns, τ_2=17.8 ns. The dramatically increased lifetimes of the co-passivated and surface-only passivated films indicate the lower defect densities due to the PFA passivation. Further, the longer lifetime of the co-passivated film than that of surface-only indicates that the GBs passivation is helpful for further inhibiting the trap-assisted recombinations, which is consistent with the higher open-circuit voltage (V_{oc}) and the FF of the corresponding PSC.[19] As reported in the literature,[9a,9f] the reduction of defects by PFA passivation in bulk perovskite films could also explain the reduced hysteresis in our work.

It should be noted that the PFA we adopt for the co-passivation strategy has actually bi-functionalities, e.g., defects passivation and moistures durability inhibition, owing to its amino and fluorocarbon chain, respectively. It varies largely from those adopted passivation agents such as quaternary ammonium,[4b] where the bearing anions might have adverse effects on the performances and stabilities of PSCs.[20] It has been reported that Lewis bases (PFA used in our work is a typical Lewis base) can form coordination with the uncoordinated

Pb.[5,14] The coordination can be probed by Fourier transform infrared spectroscopy (**Figure S13**). The FTIR analysis illustrated the reaction between PFA and perovskite resulted in the shift of the N-H peak in PFA from 1632.5 to 1644.5 cm^{-1}, while the N-H peak in perovskite has almost no change (from 1645.5 to 1644.5 cm^{-1}), which reflected the coordination of PFA with the unbonded Pb in perovskite, similar with the previous report on PVP modification of perovskite.[14] The passivation mechanism for PFA was further confirmed by XPS analysis. As shown in **Figure 2f**, there are two main peaks of $Pb_{4f7/2}$ and $Pb_{4f5/2}$ at 138.0 and 142.8 eV for films with and without PFA modification. The two small peaks located at 136.4 and 141.3 eV are ascribed to the presence of unbonded metallic Pb for the control sample.[5b,11,20] The case that the two metallic Pb peaks disappear after we added PFA (**Figure 2f**) is in agreement with the literatures,[5b,11] which ascribed to the disappearing of these two metallic peaks to the passivation effect of the Lewis bases. We thereby propose that the passivation mechanism for PFA: PFA, as a weak Lewis base, donates a lone pair of electrons on N to the empty 6p orbit of Pb on the perovskite grain surface, forming a coordination bond. We further collected the dark *I-V* characteristics of electron-only devices for calculating the trap state densities of $MAPbI_3$ films with or without PFA passivation (**Figures 2g-2i**). We found that the trap densities significantly decrease from 2.88×10^{16} to 9.34×10^{15} and 1.36×10^{15} cm^{-3} for the control, surface-only passivation and co-passivation films, respectively. This result further proves that the co-passivation is more effective than the surface-only passivation for remediating defects in the perovskite film.

It was revealed in previous studies[22] that the degradation of perovskite films was generally initialized at the defect sites at the film surface or GBs, where the perovskite molecules are more susceptible to be attacked by moisture and oxygen. Owing to the hydrophobic nature of PFA, as shown in **Figure 3a**, the addition of PFA via different routes resulted in the increase of the contact angle from 39.2° (control) to 66.8 ($MAPbI_3$/PFA-4) and 68.0° ($MAPbI_3$-PFA-4), respectively. We thus compared the moisture-resistance of the

different films by exposing them in constant temperature and humidity chamber (25°C, 50 ± 5% RH). The degradation process can be traced through the film color change (**Figures 3b-c**) and the emergence of PbI_2 (characterized by XRD, see **Figure 3d**). After the ambient exposure of 30 days, the pristine $MAPbI_3$ film completely changed to yellow color and showed a distinct PbI_2 characteristic peak, but the $MAPbI_3$-PFA-4 film still exhibited original black color and showed no impurity of PbI_2. The $MAPbI_3$/PFA-4 film showed a visible PbI_2 peak in the XRD observation (**Figure 3d**) compared to $MAPbI_3$-PFA-4, suggesting the distinguished effect of GBs passivation for improved durability. The stabilities of the PSCs with and without PFA modifications were also monitored by monitoring the unencapsulated devices in the same environment (25°C, 50 ± 5% RH), and the device performances are summarized in **Figure 3e**. The PCE of the control device quickly dropped below 20% of its initial PCE after 500 hrs, while the device with the surface-only passivation can retain over 83% of its initial PCE after 800 hrs. In contrast, the device with the co-passivation maintained 95% of the initial PCE after 800 hrs. These results conclusively confirm that films treated by co-passivation exhibited better moisture-resistance even than that of surface-only passivation, as shown in **Figure 3f**, reflecting the important role of GBs passivation on moisture durability.

Though the presented surface & GBs co-passivation strategy could result in a maximum 53.3% PCE enhancement for $MAPbI_3$ solar cell (Fig. 2b), the achieved PCE of 16.18% is still far from satisfactory (much lower than that of 20.15% achieved by Jodlowski et al[8]). To further explore if the presented co-passivation strategy is suitable for constructing higher performance PSCs, we introduced PFA in a similar manner into the cesium-containing triple cation perovskite layer, which is the main photoactive material that our laboratory is focusing on. The perovskite with a formula of $Cs_{0.05}(FA_{0.85}MA_{0.15})_{0.95}PbI_{2.55}Br_{0.45}$ (CsFAMA) was prepared according to the literature method.[1c,23] The detailed characterizations of the prepared CsFAMA film can be found in the supporting information (see the analyses of UV-Vis, PL, XPS, XRD spectra and SEM morphologies in **Figures S14-S18**). Similarly, to

confirm the incorporation of PFA into CsFAMA films, SEM-EDS analysis was performed to reveal the elements distribution. As shown in **Figures 4a-b**, the cross-section SEM images demonstrated the six layers of the solar cell architecture, and it can be seen that the distribution of F elements throughout the perovskite layer (indicated by the Pb element distribution) and the FTO layer (indicated by the Sn element distribution), which indicate the involvement of F elements at the surfaces and GBs in the perovskite layer if combing the characterizations of XPS (**Figures S15 and Figures S19**) and XRD analysis (**Figures S18**). Scanning Kelvin Probe Microscopy (SKPM) was employed again to study the passivation effect of PFA at GBs by characterizing the SP difference between GBs and inner grains of the CsFAMA films. **Figures 4c-d** exhibits the SP images of the control and CsFAMA-PFA films on FTO/TiO2 substrate. As can be clearly seen, the GBs in the control film shows 50-60 mV higher SP than that of the inner grains whereas the GBs and inner grains in the CsFAMA-PFA film only shows a less than 20 mV difference in SP (**Figure 4e**), which indicates the photo-generated charge carriers in co-passivated films can transport through the GB easily[8].

Figure 4f shows the statistics of 50 control and 80 co-passivated CsFAMA devices collected over 25 different batches. We note the improvements in all device parameters and especially in the standard deviation, which is a metric for the reproducibility: the average V_{oc} was improved from 1.07 to 1.12 V, the average J_{sc} improved from 22.88 to 23.47 mA/cm^2, the average FF improved from 71.38 to 75.98%, and the average PCE improved from 17.47 to 19.97 %. In **Figure 4g**, we show the performance of the optimized co-passivation device with the champion PCE of 21.31% and negligible hysteresis. The EQE of the champion device is shown in **Figure S20**, the integrated J_{sc} from the EQE measurement agreed well with the J_{sc} values from *J-V* measurements in **Figure 4g**. The photovoltaic parameters of the champion devices are summarized in **Table 1**. To determine the stabilized (scan speed-independent) PCEs and mimick the real working condition, we probed a CsFAMA-PFA PSC with PCE of 21.00% at its maximum power point under ambient conditions (relative humidity of 60%)

under full-sun illumination (AM 1.5G) and a constant bias voltage (**Figure 4h**). We recorded a stabilized PCE of 20.85% for CsFAMA-PFA device after 90 min. However, a CsFAMA device with the initial PCE of 17.3% degraded to 5% after 90min. The ambient stability of the CsFAMA devices by co-passivation was also examined under a high humidity condition (70 ± 5% RH). As shown in **Figure 4i**, the PCE of the CsFAMA devices was reduced to zero after 500 hrs, while the CsFAMA devices by the co-passivation still maintained 97% of their initial efficiency even after 2500 hrs.

It should be noted that the achieved 53.3% of PCEs enhancement in $MAPbI_3$ type PSCs as well as a champion PCE of 21.31% in CsFAMA type PSCs based on the presented surface & GBs co-passivation strategy are among the top in the records of the defects passivation related PSCs performance, as shown in **Table 2**.[7h,8,9a-9c,9e,9g-9h,10-13] Inspired by the highly improved performance by the copassivation of PFA, we have tried to used a series of molecules with similar structure to PFA, which have fluorocarbon chains as well as different defects passivation groups. Our current experimental results reveals that the co-passivation based on such molecules is generally able to improve the PCEs of the PSCs over 20%. These results indicate that the presented surface & GBs co-passivation strategy is universal and highly promising for accessing high performance PSCs with improved hysteresis, moisture stability and efficiency.

In summary, we have presented a simple and general co-passivation strategy that combines the advantages of both surface and GBs passivations that has been proven successful for the enhancement of the PSCs efficiency and stability. The defect densities were effectively decreased and the non-radiative recombination of the perovskite layer was much inhibited by introducing PFA much effective to decrease the defect concentrations and inhibit the non-radiative recombination. Our results in present study indicate that the co-passivation agent of PFA decorates surface and GBs throughout the depth of the films. Based on performance comparisons of the PSCs constructed by the surface-only passivation and surface

& GBs co-passivation, we can conclude that the co-passivation is much more effective for enhancing the PSCs performance than that of surface-only passivation. Owing to the hydrophobic feature of fluorocarbon chain beard in the co-passivation agent of PFA, the co-passivated CsFAMA PSCs maintained their initial efficiency even after 2500 hrs of storage in the humidity of 70 ± 5% at room temperature. The achieved 53.3% of PCEs enhancement in $MAPbI_3$ type PSCs as well as a champion PCE of 21.31% in CsFAMA type PSCs based on the presented surface & GBs co-passivation strategy, show the great potentials of present surface & GBs co-passivation strategy for boosting the PSCs performance based on the protocols of the defects manipulation.

Acknowledgement

This work was financially support by NSFC (11811530635, 51672225, 51702262, and 51872240), Science and Technology Program of Shenzhen (JCYJ20170306153027078), Natural Science Foundation of Shaanxi (2017JM5028, 2017JM2013, and 2017JQ5003), the Fundamental Research Funds for the Central Universities (G2017KY0002) and the 1000 Youth Talent Program of China. We would like to thank the Analytical & Testing Center of Northwestern Polytechnical University for XRD, AFM, and TEM characterizations. Dr. Maosen Fu is acknowledged for his help for the cross-sectional TEM-EDS measurement.

References

[1] a) H. Chen, F. Ye, W. Tang, J. He, M. Yin, Y. Wang, F. Xie, E. Bi, X. Yang, M. Grätzel, L. Han, *Nature* **2017**, *550*, 92; b) S. S. Shin, E. J. Yeom, W. S. Yang, S. Hur, M. G. Kim, J. Im, J. Seo, J. H. Noh, S. I. Seok, *Science* **2017**, *356*, 167; c) H. Tan, A. Jain, O. Voznyy, X. Lan, F. P. García de Arquer, J. Z. Fan, R. Quintero-Bermudez, M. Yuan, B. Zhang, Y. Zhao, F. Fan, P. Li, L. N. Quan, Y. Zhao. Z. Lu, Z. Yang, S. Hoogland, E. H. Sargent, *Science* **2017**, *355*, 722; d) W. S. Yang, B. W. Park, E. H. Jung, N. J. Jeon, Y. C. Kim, D. U. Lee, S. S. Shin, J. Seo, E. K. Kim, J. H. Noh, S. I. Seok, *Science* **2017**, *356*, 1376.

[2] National Center for Photovoltaics (NCPV) at the National Renewable Energy Laboratory (NREL); www.nrel.gov/pv/assets/images/efficiency-chart- 20180716.jpg.

[3] a) Q. Dong, Y. Fang, Y. Shao, P. Mulligan, J. Qiu, L. Cao, J. Huang, *Science* **2015**, *347*, 967; b) D. W. Dequilettes, S. M. Vorpahl, S. D. Stranks, H. Nagaoka, G. E. Eperon, M. E. Ziffer, H. J. Snaith, D. S. Ginger, *Science* **2015**, *348*, 683; c) D. Shi, V. Adinolfi, R. Comin, M. Yuan, E. Alarousu, A. Buin, Y. Chen, S. Hoogland, A. Rothenberger, K. Katsiev, *Science* **2015**, *347*, 519; d) J. M. Azpiroz, E. Mosconi, J. Bisquert, F. De Angelis, *Energy Environ. Sci.* **2015**, *8*, 2118; e) Q. Wang, B. Chen, Y. Liu, Y. Deng, Y. Bai, Q. Dong, J. Huang, *Energy Environ. Sci.* **2017**, *10*, 516.

[4] a) F. Wang, W. Geng, Y. Zhou, H. H. Fang, C. J. Tong, M. A. Loi, L. M. Liu, N. Zhao, *Adv. Mater.* **2016**, *28*, 9986; b) X. Zheng, B. Chen, J. Dai, Y. Fang, Y. Bai, Y. Lin, H. Wei, X. C. Zeng, J. Huang, *Nat. Energy* **2017**, *2*, 17102.

[5] a) N. K. Noel, A. Abate, S. D. Stranks, E. S. Parrott, V. M. Burlakov, A. Goriely, H. J. Snaith, *ACS Nano* **2014**, *8*, 9815; b) R. Fu, Y. Zhao, Q. Li, W. Zhou, D. Yu, Q. Zhao, *Chem. Commun.* **2017**, *53*, 1829.

[6] F. Wang, A. Shimazaki, F.Yang, K. Kanahashi, K. Matsuki, Y. Miyauchi, T. Takenobu, A. Wakamiya, Y. Murata, K. Matsuda, *J. Phys. Chem. C.* **2017**, *121*, 1562.

[7] a) D. W. deQuilettes, S. Jariwala, S. Burke, M. E. Ziffer, J. T.-W. Wang, H. J. Snaith, D. S. Ginger, *ACS Nano* **2017**, *11*, 11488; b) A. A. Mamun, T. T. Ava, H. J. Jeong, M. S. Jeong, G. Namkoong, *Phys. Chem. Chem. Phys.* **2017**, *19*, 9143; c) M. J. Simpson, B. Doughty, S. Das, K. Xiao, Y.-Z. Ma, *J. Phys. Chem. Lett.* **2017**, *8*, 3299; d) A. Merdasa, Y. Tian, R. Camacho, A. Dobrovolsky, E. Debroye, E. L. Unger, J. Hofkens, V. Sundström, I. G. Scheblykin, *ACS Nano* **2017**, *11*, 5319; e) S. Mastroianni, F. D. Heinz, J.-H. Im, W. Veurman, M. Padilla, M. C. Schubert, U. Würfel, M. Grätzel, N.-G. Park, A. Hinsch, *Nanoscale* **2015**, *7*, 19653; f) S. Draguta, S. Thakur, Y. V. Morozov, Y. Wang, J. S. Manser, P. V. Kamat, M. Kuno, *J. Phys. Chem. Lett.* **2016**, *7*, 715; g) Y. Shao, Y. Fang, T. Li, Q Wang, Q. Dong, Y. Deng, Y. Yuan, H. Wei, M. Wang, A. Gruverman, J. Shield, J. Huang, *Energy Environ. Sci.* **2016**, *9*, 1752; h) N. De Marco, H. Zhou, Q. Chen, P. Sun, Z. Liu, L. Meng, E.-P. Yao, Y. Liu, A. Schiffer, Y. Yang, *Nano Lett.* **2016**, *16*, 1009; i) Z. Chu, M. Yang, P. Schulz, D. Wu, X. Ma, E. Seifert, L. Sun, K. Zhu, X. Li, K Lai, *Nat. Commun.* **2017**, *8*, 2230; j) J. S. Yun, A. Ho-Baillie, S Huang, S. H. Woo, Y. Heo, J. Seidel, F. Huang, Y.-B. Cheng, M. A. Green, *J. Phys. Chem. Lett.* ***2015****, 6,* 875.

[8] A. D. Jodlowski, C. Roldán-Carmona, G. Grancini, M. Salado, M. Ralaiarisoa, S. Ahmad, N. Koch, L. Camacho, G. de Miguel, M. K. Nazeeruddin, *Nat. Energy* **2017**, *2*, 972.

[9] a) J. Xu, A. Buin, A. H. Ip, W. Li, O. Voznyy, R. Comin, M. Yuan, S. Jeon, Z. Ning, J. J. McDowell, P. Kanjanaboos, J.-P. Sun, X. Lan, L. N. Quan, D. H. Kim, I. G. Hill, P. Maksymovych, E. H. Sargent, *Nat. Commun.* **2015**, *6*, 7081; b) X. Li, M. I. Dar, C. Yi, J. Luo, M. Tschumi, S. M. Zakeeruddin, M. K. Nazeeruddin, H. Han, M. Grätzel, *Nat. Chem.* **2015**, *7*, 703; c) D. Bi, P. Gao, R. Scopelliti, E. Oveisi, J. Luo, M. Grätzel, A. Hagfeldt, M. K. Nazeeruddin, *Adv. Mater.* **2016**, *28*, 2910; d) Q. Chen, H. Zhou, T.-B. Song, S. Luo, Z. Hong, H.-S. Duan, L. Dou, Y. Liu, Y. Yang, *Nano Lett.* **2014**, *14*,

4158; e) X. Liu, F. Lin, C.-C. Chueh, Q. Chen, T. Zhao, P.-W. Liang, Z. Zhu, Y. Sun, A. K.-Y. Jen, *Nano Energy* **2016**, *30*, 417; f) Y. Shao, Z. Xiao, C. Bi, Y. Yuan, J. Huang, *Nat. Commun.* **2014**, *5*, 5784; g) Y. Guo, W. Sato, K. Shoyama, H. Halim, Y. Itabashi, R. Shang, E. Nakamura, *J. Am. Chem. Soc.* **2017**, *139*, 9598; h) D. S. Lee, J. S. Yun, J. Kim, A. M. Soufiani, S Chen, Y. Cho, X. Deng, J. Seidel, S. Lim, S. Huang, A. W. Y. Ho-Baillie, *ACS Energy Lett.* **2018**, *3*, 647.

[10] L. Liu, S. Huang, Y. Lu, P. Liu, Y. Zhao, C. Shi, S. Zhang, J. Wu, H. Zhong, M. Sui, H. Zhou, H. Jin, Y. Li, and Q. Chen, *Adv. Mater.,* **2018**, 30, 1800544.

[11] D. Bi, C. Yi, J. Luo, J.-D. Décoppet, F. Zhang, S. M. Zakeeruddin, X. Li, A. Hagfeldt, M. Grätzel, *Nat. Energy* **2016**, *1*, 16142.

[12] T. Niu, J Lu, R. Munir, J. Li, D. Barrit, X. Zhang, H. Hu, Z. Yang, A. Amassian, K. Zhao, S. F. Liu, *Adv. Mater.* **2018,** *30,* 1706576.

[13] Y. Guo, J. Ma, H. Lei, F. Yao, B. Li, L. Xiong, G. Fang, *J. Mater. Chem. A,* **2018**, *6*, 5919.

[14] L. Zuo, H. Guo, D. W. deQuilettes, S. Jariwala, N. De Marco, S. Dong, R. DeBlock, D. S. Ginger, B. Dunn, M. Wang, Y. Yang, *Sci. Adv.* **2017**, *3*, e1700106.

[15] M. U. Rothmann, W. Li, Y. Zhu, U. Bach, L. Spiccia, J. Etheridge, Y.-B. Cheng, *Nat. Commun.* **2017**, *8*, 14547; A. Alberti, I. Deretzis, G. Pellegrino, C. Bongiorno, E. Smecca, G. Mannino, F. Giannazzo, G. G. Condorelli, N. Sakai, T. Miyasaka, C. Spinella , A. L. Magna. Chemphyschem. **2015**, *16*, 3064.

[16] a) Y. Zhao, J. Wei, H. Li, Y. Yan, W. Zhou, D. Yu, Q. Zhao, *Nat. Commun.* **2016**, *6*, 10228; b) J. Wei, H. Li, Y. Zhao, W. Zhou, R. Fu, Y. Leprince-Wang, D. Yu, Q. Zhao, *Nano Energy* **2016**, *26*, 139.

[17] M. Cha, P. Da, J. Wang, W. Wang, Z. Chen, F. Xiu, G. Zheng, Z.-S. Wang, *J. Am. Chem. Soc.* **2016**, *138*, 8581.

[18] H. Cho, S.-H. Jeong, M.-H. Park, Y.-H. Kim, C. Wolf, C.-L. Lee, J. H. Heo, A.

Sadhanala, N. Myoung, S. Yoo, S. H. Im, R. H. Friend, T.-W. Lee, *Science* **2015**, *350*, 1222.

[19] D. Bi, W. Tress, M. I. Dar, P. Gao, J. Shan, C. Renevier, K. Schenk, A. Abate, F. Giordano, J.-P. C. Baena, J.-D. Décoppet, S. M. Zakeeruddin, M. K. Nazeeruddin, M. Grätzel, A. Hagfeldt, *Sci. Adv.* **2016**, *2*, e1501170.

[20] Z. Li, C. Xiao, Y. Yang, S. P. Harvey, D. H. Kim, J. A. Christians, M. Yang, P. Schulz, S. U. Nanayakkara, C.-S. Jiang, J. M. Luther, J. J. Berry, M. C. Beard, M. M. Al-Jassim, K. Zhu, *Energy Environ. Sci.* **2017***, 10,* 1234.

[21] R. Lindblad, D. Bi, B.-W. Park, J. Oscarsson, M. Gorgoi, H. Siegbahn, M. Odelius, E. M. J. Johansson, H. Rensmo, *J. Phys. Chem. Lett.* **2014**, *5*, 648.

[22] Q. Wang, B. Chen, Y. Liu, Y. Deng, Y. Bai, Q. Dong, J. Huang, *Energy Environ. Sci.* **2016**, *10*, 516.

[23] a) M. Saliba, T. Matsui, K. Domanski, J.-Y. Seo, A. Ummadisingu, S. M. Zakeeruddin, J.-P. Correa-Baena, W. R. Tress, A. Abate, A. Hagfeldt, M. Grätzel, *Science* **2016**, *354*, 206; b) M. Saliba, T. Matsui, J.-Y. Seo, K. Domanski, J.-P. Correa-Baena, M. K. Nazeeruddin, S. M. Zakeeruddin, W. R. Tress, A. Abate, A. Hagfeldt, M. Grätzel, *Energy Environ. Sci.* **2016**, *9*, 1989.

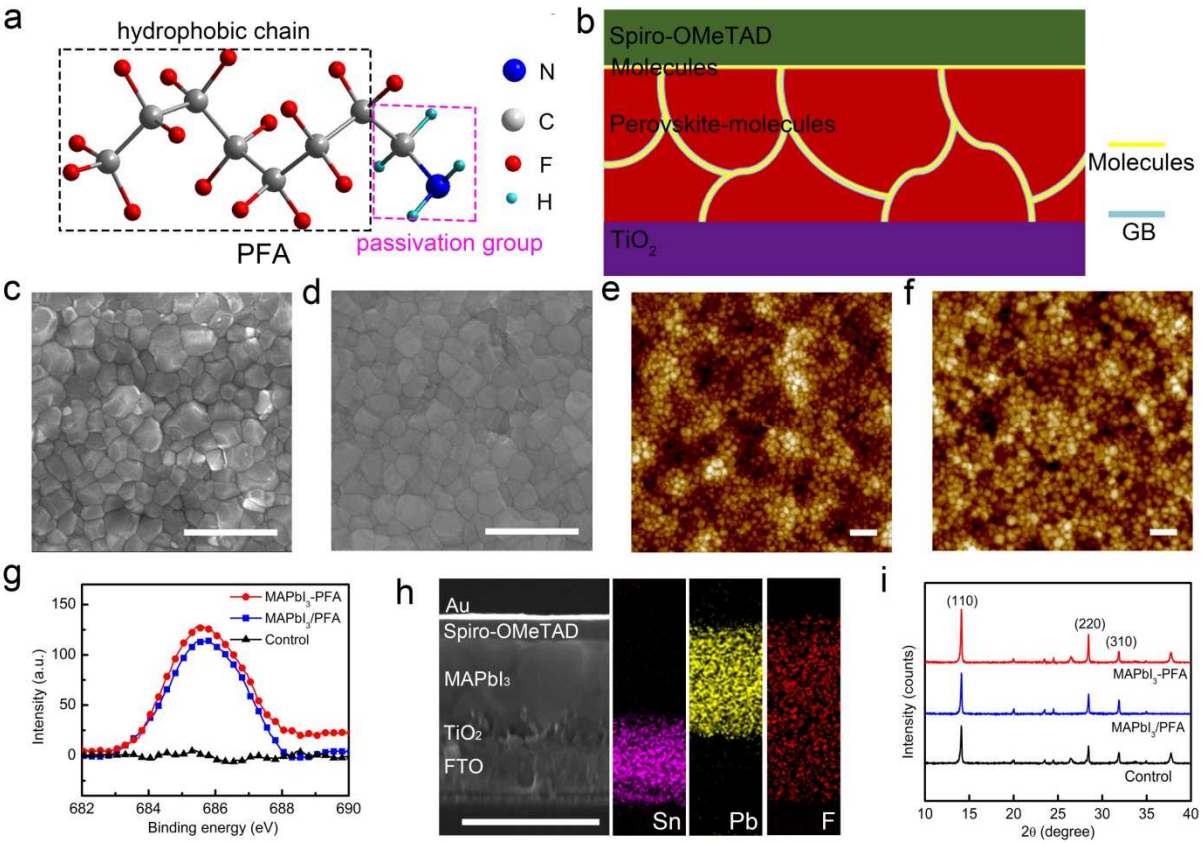
a
hydrophobic chain
PFA
passivation group
N
C
F
H
b
Spiro-OMeTAD
Molecules
Perovskite-molecules
TiO2
Molecules
GB
c
d
e
f
g
MAPbI3-PFA
MAPbI3/PFA
Control
Intensity (a.u.)
Binding energy (eV)
h
Au
Spiro-OMeTAD
MAPbI3
TiO2
FTO
Sn
Pb
F
i
(110)
(220)
(310)
MAPbI3-PFA
MAPbI3/PFA
Control
Intensity (counts)
2θ (degree)

Figure 1

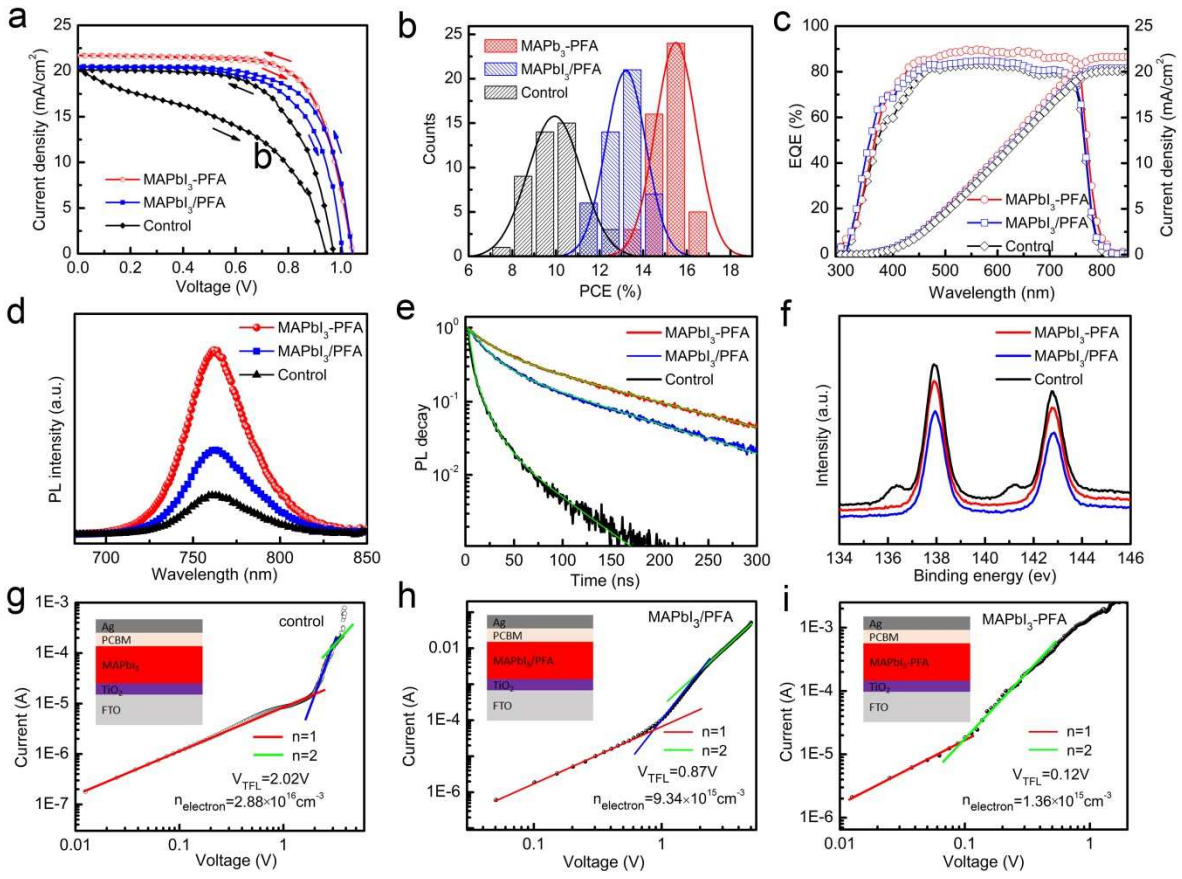
a
Current density (mA/cm^2)
Voltage (V)
MAPbI$_3$-PFA
MAPbI$_3$/PFA
Control
b
b
Counts
PCE (%)
MAPb$_3$-PFA
MAPbI$_3$/PFA
Control
c
EQE (%)
Current density (mA/cm^2)
Wavelength (nm)
MAPbI$_3$-PFA
MAPbI$_3$/PFA
Control
d
PL intensity (a.u.)
Wavelength (nm)
MAPbI$_3$-PFA
MAPbI$_3$/PFA
Control
e
PL decay
Time (ns)
MAPbI$_3$-PFA
MAPbI$_3$/PFA
Control
f
Intensity (a.u.)
Binding energy (ev)
MAPbI$_3$-PFA
MAPbI$_3$/PFA
Control
g
control
Ag
PCBM
MAPbI$_3$
TiO$_2$
FTO
Current (A)
Voltage (V)
n=1
n=2
V_{TFL}=2.02V
$n_{electron}$=2.88×10^{16}cm^{-3}
h
MAPbI$_3$/PFA
Ag
PCBM
MAPbI$_3$/PFA
TiO$_2$
FTO
Current (A)
Voltage (V)
n=1
n=2
V_{TFL}=0.87V
$n_{electron}$=9.34×10^{15}cm^{-3}
i
MAPbI$_3$-PFA
Ag
PCBM
MAPbI$_3$-PFA
TiO$_2$
FTO
Current (A)
Voltage (V)
n=1
n=2
V_{TFL}=0.12V
$n_{electron}$=1.36×10^{15}cm^{-3}

Figure 2

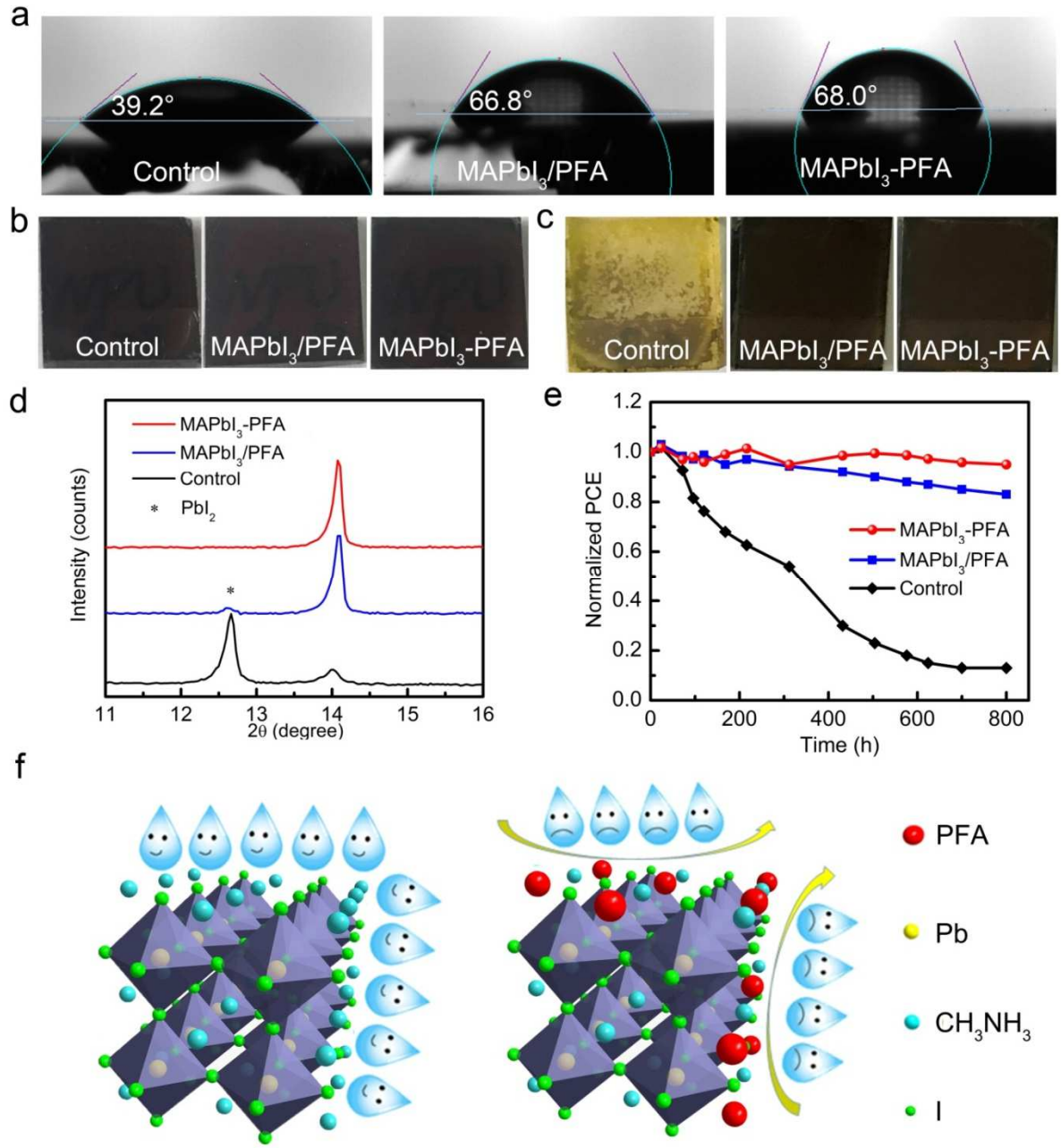
a
39.2°
Control
66.8°
MAPbI3/PFA
68.0°
MAPbI3-PFA
b
Control
MAPbI3/PFA
MAPbI3-PFA
c
Control
MAPbI3/PFA
MAPbI3-PFA
d
MAPbI3-PFA
MAPbI3/PFA
Control
* PbI2
Intensity (counts)
2θ (degree)
e
Normalized PCE
Time (h)
MAPbI3-PFA
MAPbI3/PFA
Control
f
PFA
Pb
CH3NH3
I

Figure 3

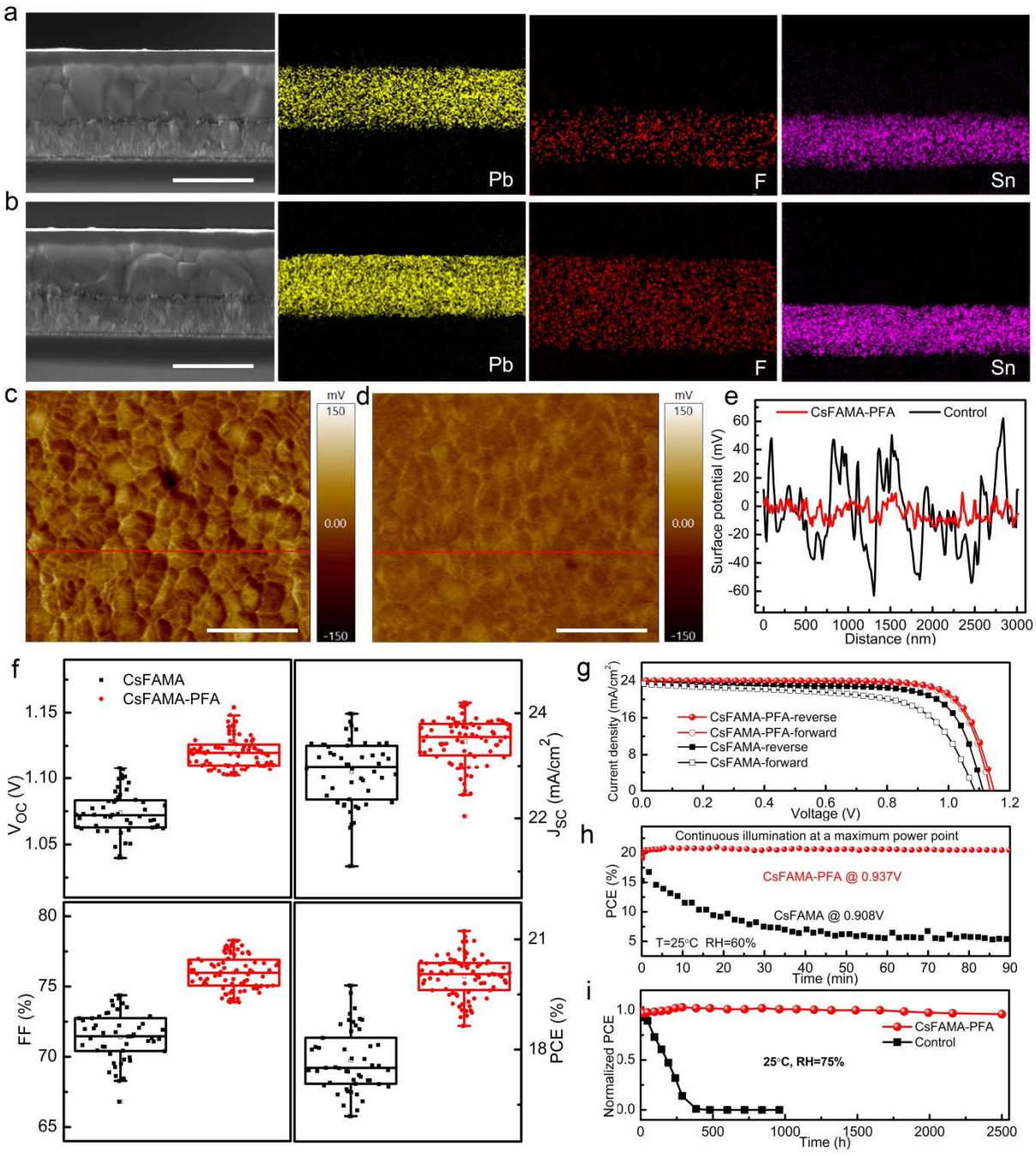
a
Pb
F
Sn
b
Pb
F
Sn
c
mV
150
0.00
-150
d
mV
150
0.00
-150
e
CsFAMA-PFA
Control
Surface potential (mV)
Distance (nm)
f
CsFAMA
CsFAMA-PFA
V_{OC} (V)
J_{SC} (mA/cm^2)
FF (%)
PCE (%)
g
CsFAMA-PFA-reverse
CsFAMA-PFA-forward
CsFAMA-reverse
CsFAMA-forward
Current density (mA/cm^2)
Voltage (V)
h
Continuous illumination at a maximum power point
CsFAMA-PFA @ 0.937V
CsFAMA @ 0.908V
T=25°C RH=60%
PCE (%)
Time (min)
i
CsFAMA-PFA
Control
25°C, RH=75%
Normalized PCE
Time (h)

Figure 4

Table 1

Sample	Scan direction	J_{SC} (mA/cm^2)	V_{OC} (V)	FF (%)	Champion PCE (%)
Control	Forward	23.42	1.09	64.55	16.48
	Reverse	23.42	1.11	75.16	19.53
Co-passivation	Forward	24.06	1.13	78.26	21.28
	Reverse	24.10	1.14	77.56	21.31

Table 2

Passivants	Average PCE before passivation (%)	Average PCE after passivation (%)	Enhancement rate (%)	Champion PCE (%)	Cell area (mm^2)	Ref.
Guanidinium	15.8/17.0	16.3/19.2	3.3/12.9	17.13/20.15	10.80	[7h, 8]
PCBM	12.0	13.6	13.3	14.4	4.90	[9a]
ω-ammonium chlorides	8.1	15.2	**89.8**	16.7	4.80	[9b]
FEAI	15.6	17.9	15.0	18.0	16.00	[9c]
DF-C_{60}	15.7	18.1	15.6	18.5	3.14	[9e]
Citric acid	13.2	16.8	27.0	17	4.00	[9g]
PEAI	16.5	14.3	-13.3	-	15.90	[9h]
IT-4F	15.2	17.6	15.8	18.3	9.00	[10]
PMMA	~20.0	**21.0**	~5.0	**21.6**	10.51	[11]
PCBM, ITIC, DTS, and DR3T	16.7	17.3/18.0/17.4/18.2	3.5/7.8/4.2/9.0	18.4/19.0/18.5/ 19.3	9.00	[12]
MMI	17.13	19.18	12	20.1	10.2	[13]
PFA ($MAPbI_3$)	10.12	15.51	**53.3**	16.18	10.00	Our work
PFA (CsFAMA)	17.47	**19.97**	14.3	**21.31**	10.00	Our work

Figure Captions:

Figure 1. (a) (a) Molecular structure of PFA. (b) Scheme illustration of the surface & GBs co-passivation by using PFA. (c-d) SEM and (e-f) AFM observations of the films by surface-only passivation and co-passivation. (g) Binding energy of F1s in XPS spectra for different films. (h) Cross-section SEM image and corresponding SEM-EDS mappings of the MAPbI3-PFA device. (i) XRD patterns of the different films. The scale bar is 1 μm.

Figure 2. (a) *J-V* curves in both reverse and forward directions, **(b)** PCE distribution, **(c)** EQE curves of the champion devices. **(d)** Steady-state PL spectra, **(e)** Time-resolved PL measurement, and **(f)** XPS surface spectra of Pb_{4f} for different films: $MAPbI_3$ (control), $MAPbI_3$/PFA-4 (surface-only passviation), and $MAPbI_3$-PFA-4 (surface & GBs co-passiation). Dark *I-V* measurement of the electron-only devices displaying V_{TFL} (V_{TFL} is the onset voltage of the trap-filled limit region) kink point behavior for the (g) $MAPbI_3$, (h) $MAPbI_3$/PFA, and (i) $MAPbI_3$-PFA films.

Figure 3. (a) Contact angles, **(b)** images of pristine, **(c)** images after exposure in moisture air (50 ± 5 RH %, 25˚C), and **(d)** XRD patterns of different films exposed under 50 ± 5 % RH at 25˚C after 30 days: $MAPbI_3$ (control), $MAPbI_3$/PFA-4 (surface-only passivation), and $MAPbI_3$-PFA-4 (surface & GBs co-passiation). **(e)** Normalized PCEs of different devices as a function of storage time in ambient condition with a relatively humility of 50 ± 5 %: $MAPbI_3$, $MAPbI_3$/PFA-4 and $MAPbI_3$-PFA-4. **(f)** Schematic illustration of the moisture tolerance of the $MAPbI_3$-PFA structures.

Figure 4. SEM-EDS mappings of Pb, F and Sn for different devices: **(a)** CsFAMA and **(b)** CsFAMA-PFA. SKPM images of **(c)** CsFAMA and **(d)** CsFAMA-PFA films. **(e)** The SP values varied with distance were recorded from the red solid lines in **(c)** and **(d)**. The scale bar is 1 μm. **(g)** PCEs statistics from 80 devices (25 different batches) for different devices:

CsFAMA (50 devices) and CsFAMA-PFA. **(h)** J-V curves of the champion PSC for CsFAMA and CsFAMA-PFA measured in both reverse and forward directions. **(i)** Photostability tests under AM 1.5G illumination for the unencapsulated CsFAMA and CsFAMA-PFA devices. **(d)** Normalized PCEs for the CsFAMA and CsFAMA-PFA devices as a function of storage time in ambient condition with a relative humility of 70 ± 5%.

Table 1 Photovoltaic parameters of CsFAMA based perovskite devices before and after co-passivation.

Table 2 Summary of GBs passivation related PSCs performance improvement collected from the most-recent literatures.

TOC

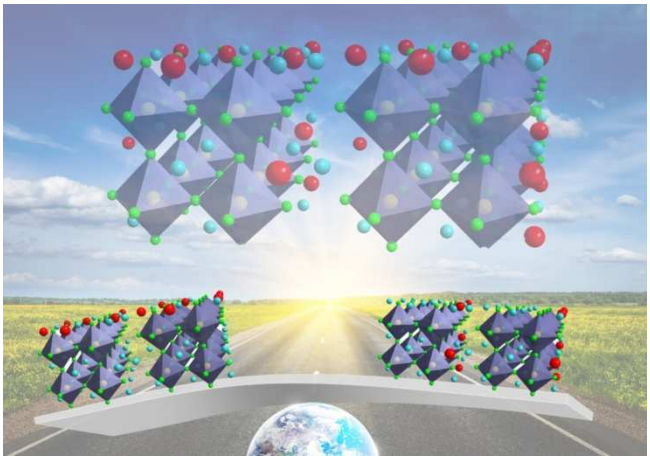

A new way of accessing perovskite solar cells (PSCs) with highly improved efficiency and stability is demonstrated by developing a surface & grain boundaries co-passivation strategy, which achieved 53.3% of efficiency enhancement in $MAPbI_3$ type PSCs and 21.31% of champion efficiency in CsFAMA type PSCs.

Supporting Information

Surface & Grain Boundaries Co-passivation by Fluorocarbon based Bifunctional Molecules for Perovskite Solar Cells with Efficiency Over 21%

Pengfei Guo, Qian Ye*, Xiaokun Yang, Jin Zhang, Fei Xu, Dmitry Shchukin, Bingqing Wei, Hongqiang Wang*

Mr. P. Guo, Dr. Q. Ye, Mr. X. Yang, Ms. J. Zhang, Dr. F. Xu, Prof. B. Wei, Prof. H. Wang
State Key Laboratory of Solidification Processing, Center for Nano Energy Materials, School of Materials Science and Engineering, Northwestern Polytechnical University and Shaanxi Joint Laboratory of Graphene (NPU), Xi'an, 710072, P. R. China
Dr. Q. Ye
Research & Development Institute of Northwestern Polytechnical University in Shenzhen, Northwestern Polytechnical University, Xi'an, 710072, P. R. China
Prof. D. Shchukin,
Stephenson Institute for Renewable Energy, Department of Chemistry, University of Liverpool, Crown Street, Liverpool, L69 7ZD, United Kingdom
Prof. B. Wei
Department of Mechanical Engineering, University of Delaware, Newark, Delaware 19716, United States
Prof. Q. Meng

Email: yeqian213@nwpu.edu.cn; hongqiang.wang@nwpu.edu.cn

Experimental

Materials

Unless stated otherwise, all materials were purchased from Sigma-Aldrich and used as received. Fuorine-doped tin oxide (FTO) glass substrates (around 1.5 cm×1.5 cm) were obtained from Pilkington and etched by a commercial corporation. Spiro-OMeTAD (2,2',7,7'-Tetrakis[N,N-di(4-methoxyphenyl)amino]-9, 9'-spirobifuorene, ≥99.8% purity), 4-tert-butylpyridine (tBP, ≥99.9% purity) and lithium-bis(trifluoromethanesulfonyl)imide (Li–TFSI, ≥99.9% purity) were supplied by Xi'an Polymer Light Technology Corp. 1H,1H-Perfluorooctylamine (PFA, ≥99.9% purity) was bought from Alfa Aesar.

Device fabrication

The etched FTO substrates were cleaned sequentially in Hellmanex detergent, acetone and ethanol, isopropyl alcohol, dried with a compressed nitrogen gun, and finally treated under an oxygen plasma for 10 min to remove the last traces of organic residues. A ~50 nm thick TiO_2 compact layer was then spin-coated onto the FTO substrate at 2000 rpm for 60 s using an acidic titanium diisopropoxidebis (acetylacetonate) solution (75% in 2-propanol) diluted in ethanol (1:39, volume ratio) as the precursor, followed by drying at 150 °C for 10 min and annealing at 500 °C for 30 min in air.

Fabrication of perovskite films with surface & GBs co-passivation: (1) $MAPbI_3$. A 1.2 M $MAPbI_3$ precursor solution of PbI_2 (1.2 M) and MAI (1.2 M) was stirred in a mixture of DMF and DMSO (4:1 v/v) at 60 °C for 2 h; (2) $Cs_{0.05}FA_{0.81}MA_{0.14}PbI_{2.55}Br_{0.45}$. A1.2 M "mixed" perovskite precursor solutions containing CsI (0.06M) FAI (0.97 M), PbI_2 (0.97 M), MABr (0.17 M) and $PbBr_2$ (0.17M) was stirred in a mixture of DMF and DMSO (4:1 v/v) at 60 °C for 2 h. The resulting solution was coated onto the FTO/TiO_2 substrate in an argon glovebox by a consecutive two-step spin-coating process at 1,000 and 4,000 r.p.m for 10 and 30 s, respectively. During the second step, 200 μL PFA with different concentrations (0.6, 1.2, 2.4,

6.0 and 15 mg/mL) in chlorobenzene was immediately poured on the spinning substrate 10 s prior to the end of the program. Thereafter, the substrate was put onto a hotplate for 60 min at 100 °C, forming the $MAPbI_3$-molecule film and the $Cs_{0.05}FA_{0.81}MA_{0.14}PbI_{2.55}Br_{0.45}$- molecule film.

Fabrication of perovskite film with surface-only passivation: PFA solution with different concentrations (0.6, 1.2, 2.4, 6.0 and 15 mg/mL) in chlorobenzene was spin coated onto the preformed $MAPbI_3$ and $Cs_{0.05}FA_{0.81}MA_{0.14}PbI_{2.55}Br_{0.45}$ perovskite layer at 3000 rpm for 30 s followed by annealing at 70 °C for 10 min, forming the $MAPbI_3$/ molecule film and the $Cs_{0.05}FA_{0.81}MA_{0.14}PbI_{2.55}Br_{0.45}$/ molecule film.

Fabrication of perovskite film with PFA molecules in the precursors: the molecule was added into DMF with a concentration 6.0 mg/mL forming a DMF-molecule mixed solution. A 1.2 M $MAPbI_3$ precursor solution of PbI_2 (1.2 M) and MAI (1.2 M) was stirred in a mixture of DMF-molecule and DMSO (4:1 v/v) at 60 °C for 2 h forming the molecule involved $MAPbI_3$ film ($MAPbI_3$+ molecule).

After cooling down to room temperature, the HTM solution was then deposited by spin coating at 5,000 r.p.m. for 30 s. The HTM solution was prepared by dissolving 72.3 mg Spiro-MeOTAD, 28.8 mL tBP and 17.5 mL of a stock solution of 520 mg/mL Li-TFSI in acetonitrile in 1 mL chlorobenzene. The samples were then aged in a desiccator for ~12 hrs. Finally, the Au counter electrode was deposited by thermal evaporation. The active area of this electrode was 0.1 cm^2, which was calculated by a mask plate and further determined by an optical microscope.

Device characterization

Simulated AM 1.5G irradiation (100 mW cm^{-2}) was produced by a xenon-lamp-based solar simulator (Oriel 67005, 150 W Solar Simulator) for current density-voltage *(J-V)* measurements. The light intensity was calibrated by a silicon (Si) diode (Hamamatsu S1133)

equipped with a Schott visible-colour glass filter (KG5 colour-filter). A Keithley 2420 Source-Meter was used for *J-V* measurement. The scanning rate was 0.2V/s with no device preconditioning, such as light soaking or extended forward voltage biasing in the dark before starting the measurement. The dark *I-V* characteristics of the electron-only devices were measured by a Keithley 2420 source, and the trap density was caculated using a previous method[1]. For the steady-state output measurement, the solar cells were put under the simulated AM1.5-G, 1-sunillumination to record the photocurrent under the bias of 0.937 and 0.908 V. External quantum efficiency (EQE) curves were characterized with a Newport QE measurement kit by focusing a monochromatic beam of light onto the devices. The morphology and structure of the samples were characterized by a field emission SEM with an EDS detector (FEI Nova) and an atomic force microscope (AFM, Bruker Dimension Icon). Scanning Kelvin Probe Microscopy (SKPM) measurements were performed on an Asylum Research MFP-3D-Origin AFM using Au-coated Si conductive probes (HA_HR, NT-MDT). TEM was performed in combination with EDS by using an FEI Tecnai F30 equipped with a field emission gun (FEG) operated at 300 kV, a high angle annular dark field (HAADF) STEM detector, and an Oxford Instruments EDS detector with an ultra-thin window. Focused ion beam (FIB) was used to prepare the cross sections of perovskite devices. X-ray diffraction (XRD) spectra were recorded on a PANAlyticalX'pert PRO equipped with a diffracted beam monochromator, and a conventional cobalt target X-ray tube set to 40 kV and 30 mA. X-ray photoelectron spectroscopy (XPS) depth profile measurements were conducted on a PHI Versa Probe II XPS system equipped with a small spot X-ray beam, automated charge compensation, monatomic and cluster ion guns (Ar+, C60, Arcluster), heating/cooling stage and angle-resolved XPS. The FTIR spectra (4000 to 500 cm^{-1}) were recorded on a Jasco FT/IR-6100 FTIR. The absorption was measured using the ultraviolet-visible (UV-vis) spectrophotometer (Perkin-Elmer Lambda 35 UV-vis-NIR). The steady-state photoluminescence spectra were measured using pulse laser as an optical excitation source

(wavelength: 470 nm, Horiba FluorologFL-3), and time-resolved photoluminescence (TRPL) experiments were simultaneously performed by exciting at 470 nm. The contact angles were measured on a Data physics OCA-20 contact-angle system at ambient temperature. Electrochemical impedance spectroscopy (EIS) was executed on a homemade electrochemical workstation. The EIS was measured under illumination of AM1.5G simulated solar light (100 mW cm-2) at 0.8V in a frequency range of 10 Hz-1 MHz. Moisture-stability measurements were performed in a constant temperature & humidity incubator in dark.

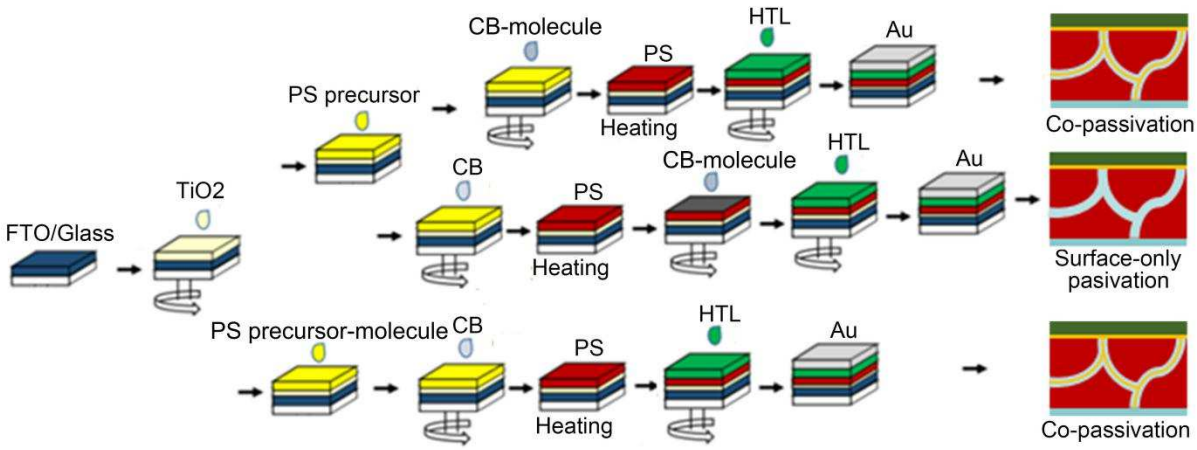

Scheme S1. Schematic illustration of the fabrication procedures for the Perovskite solar cells with different expected passivation: (A) Surface & GBs co-passivation; (B Surface-only passivation; (C) Surface & GBs co-passivation.

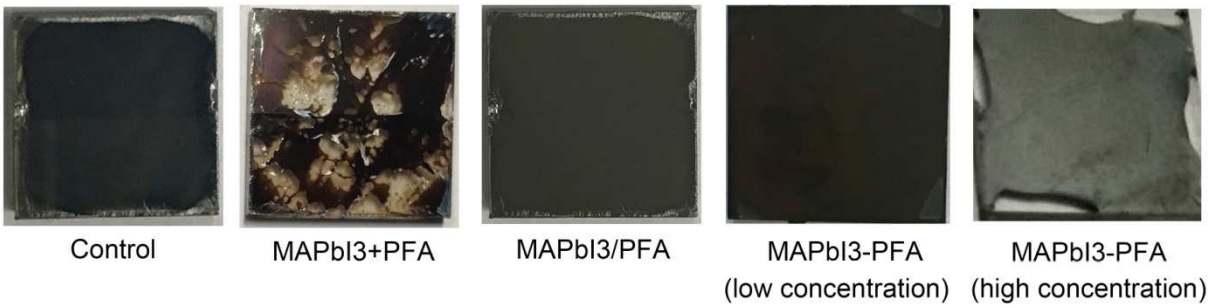

Figure S1 The optical images of different perovskite films: $MAPbI_3$ (control), $MAPbI_3$+PFA (adding into the precursor), $MAPbI_3$/PFA-4 (Surface-only passivation), $MAPbI_3$-PFA-4 (surface & GBs passivation), and $MAPbI_3$-PFA (50mg/ml in CB, surface & GBs passivation). The co-passivated film with a low concentration of PFA demonstrated continuous and complete coverage, while using of a higher concentration of PFA resulted in films with large pinholes and bad coverage.

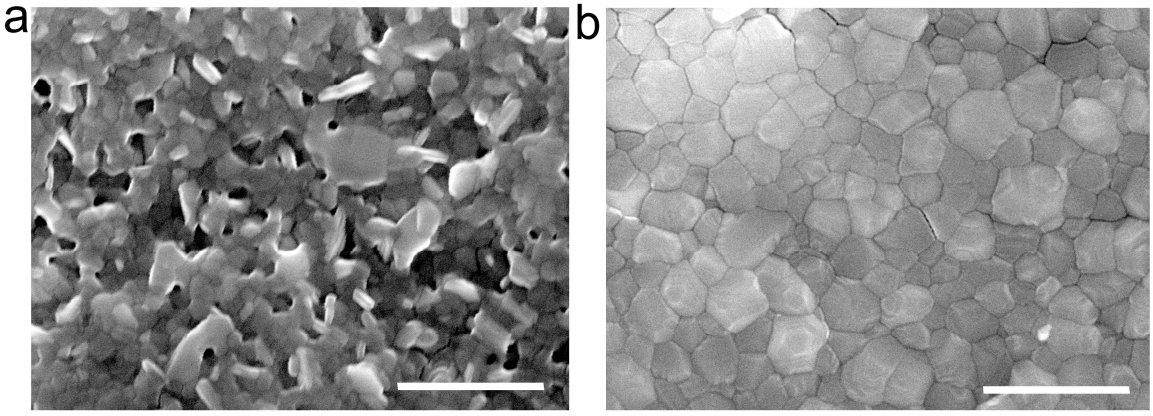

Figure S2 The SEM images of different perovskite films: **(a)** $MAPbI_3$+PFA-4 (adding PFA in precursors), **(b)** $MAPbI_3$ (control). The scale bar is 1 μm.

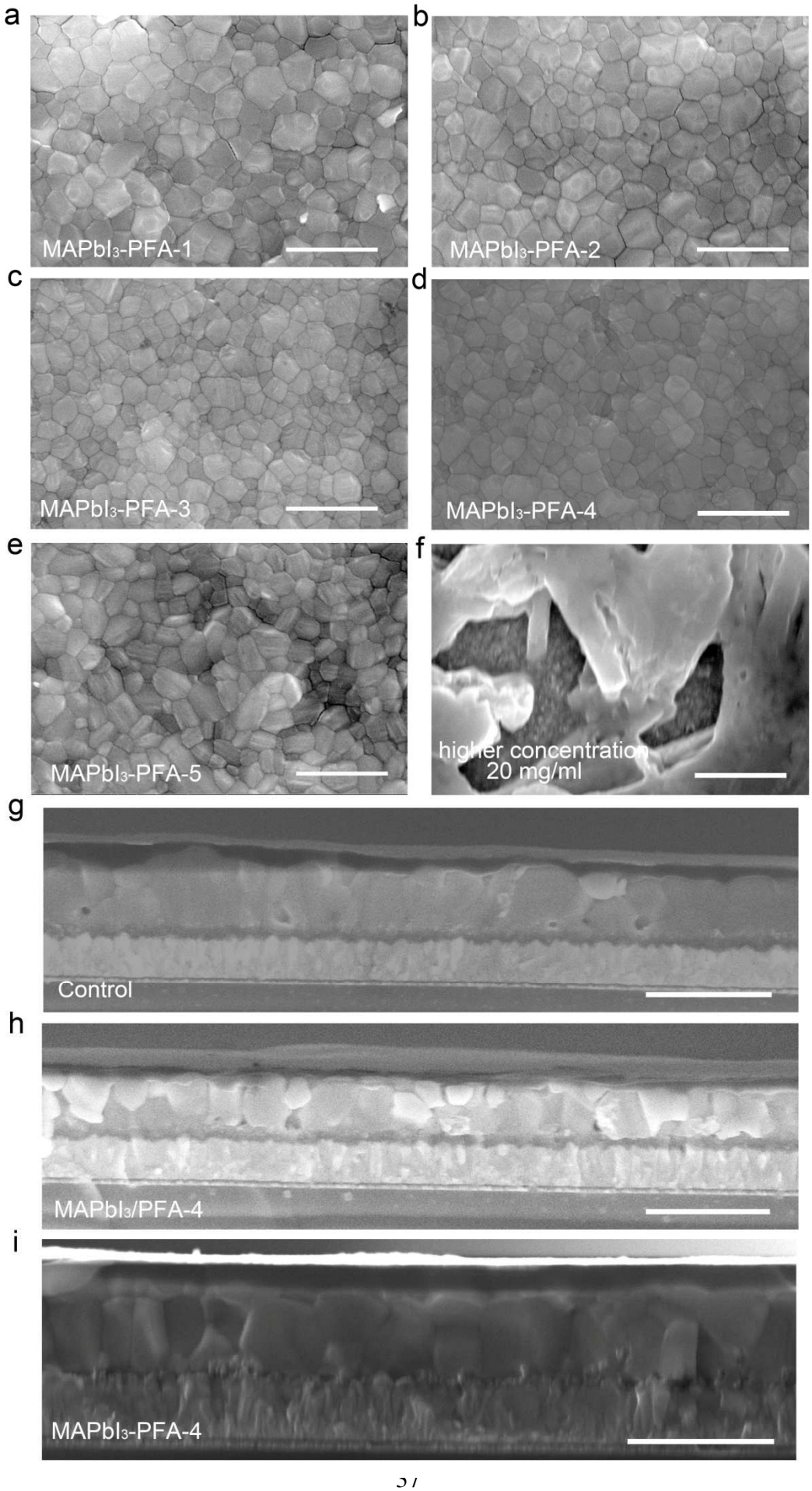
a
MAPbI3-PFA-1
b
MAPbI3-PFA-2
c
MAPbI3-PFA-3
d
MAPbI3-PFA-4
e
MAPbI3-PFA-5
f
higher concentration
20 mg/ml
g
Control
h
MAPbI3/PFA-4
i
MAPbI3-PFA-4

Figure S3 Surface morphologies of the co-passivated perovskite films with different PFA concentrations: **(a)** $MAPbI_3$-PFA-1, **(b)** $MAPbI_3$-PFA-2, **(c)** $MAPbI_3$-PFA-3, **(d)** $MAPbI_3$-PFA-4, **(e)** $MAPbI_3$-PFA-5, and **(f)** $MAPbI_3$-PFA with a high concentration ((20mg/ml in CB). Cross-sectional SEM images of different devices: **(g)** $MAPbI_3$ (control), **(h)** $MAPbI_3$/PFA-4 (surface-only passivation), and **(i)** $MAPbI_3$-PFA-4 (co-passivation). The scale bar is 1 μm. The co-passivated film with a low concentration of PFA (<6mg/ml in CB) has little influence on the morphological change comparing to the control film, while using a higher concentration of PFA (>20mg/ml in CB) resulted in films with large pinholes and bad coverage.

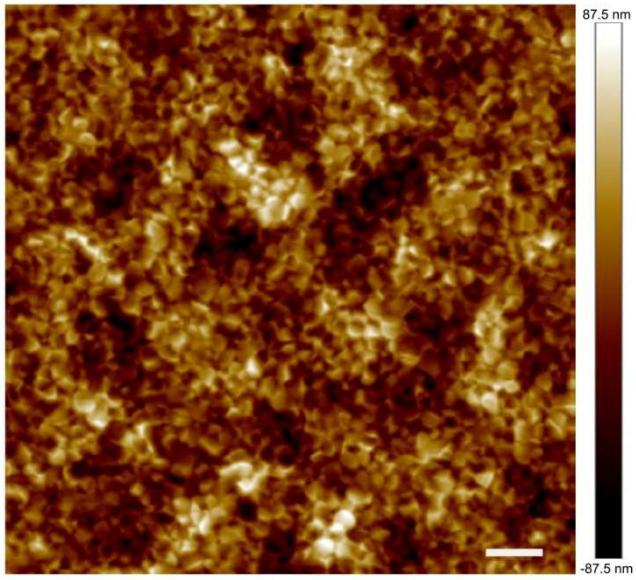

Figure S4 AFM image of the control film. The scale bar is 1 μm.

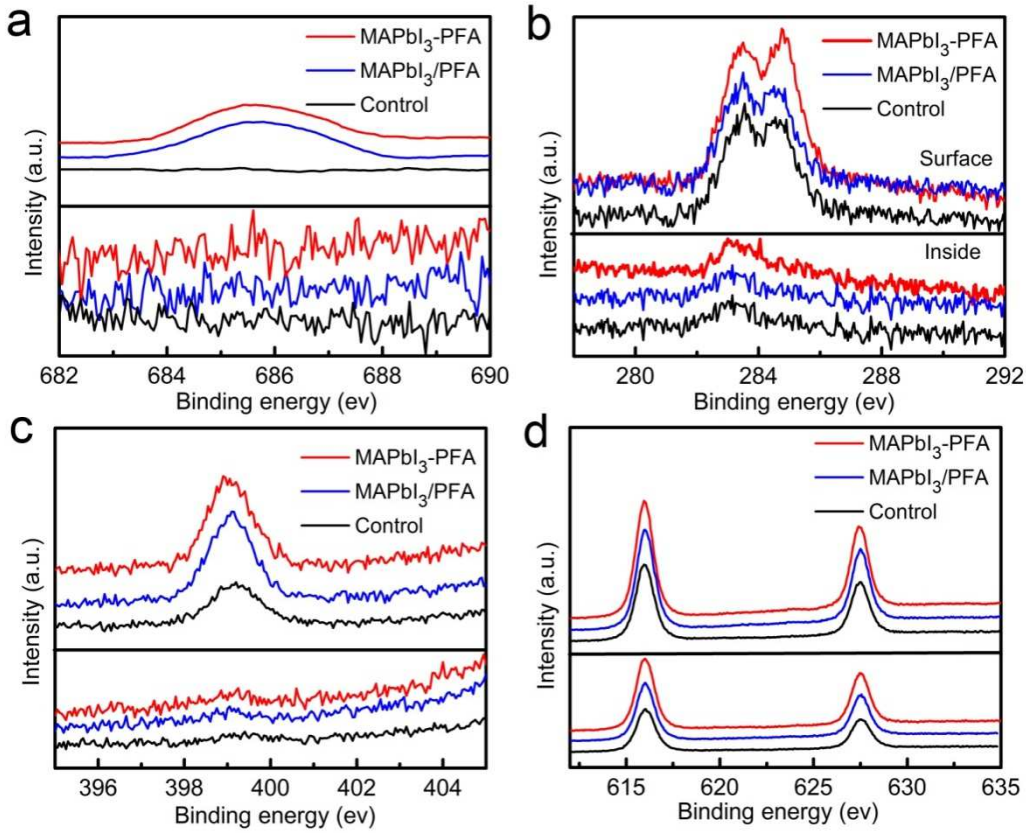

Figure S5 Binding energies of **(a)** F_{1s}, **(b)** N_{1s}, **(c)** C_{1s}, and **(d)** I_{3d} in surface and in-depth profile XPS spectra for the control ($MAPbI_3$), $MAPbI_3$-PFA, and $MAPbI_3$-PF films. The measured depth is about 20 nm (etch rate ≈ 0.1 nm/s, 200s).

As we assume that Routes A and C result in different distributions of PFA in the perovskite layer (see **Scheme S1**), X-ray photoelectron spectroscopy (XPS) was employed to experimentally verify the exact location of PFA in each resulted film. As shown in **Figure 1g**, the evident peak of F_{1s} located at around 685.7 eV can be found for both $MAPbI_3$-PFA and $MAPbI_3$/PFA films, illustrating the existence of PFA molecules on the surface of the both films. As we expect only the $MAPbI_3$-PFA film has PFA inside, XPS depth profile was further investigated to explore the depth distribution difference of F element between the two type films. However, signals of F_{1s} were not detected for both films. Detailed investigation reveals that signals of N_{1s} and C_{1s} have also been found in film surface but not inside, reflecting that the missed detection of F element deep in the $MAPbI_3$-PFA film might be due

to the removing of light elements by the high energy Ar ion beam during the XPS depth profile characterization.

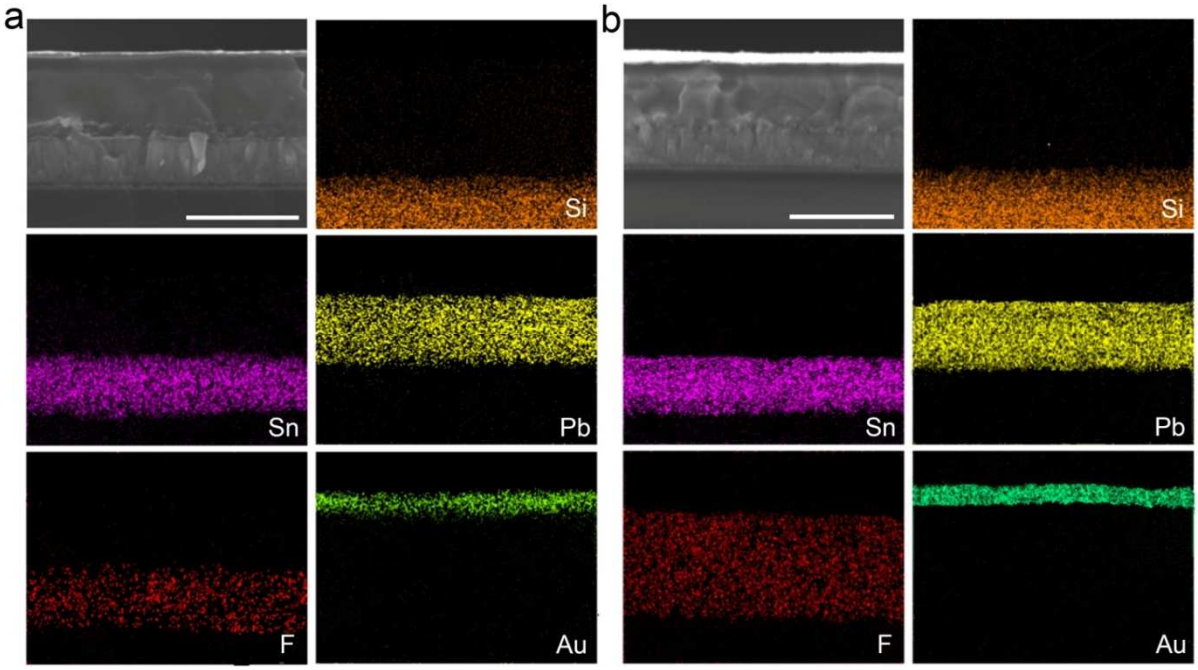

Figure S6 Cross-sectional SEM images and corresponding SEM-EDS mappings (Pb, F, and Sn) of **(a)** $MAPbI_3$/PFA and **(b)** $MAPbI_3$-PFA devices.

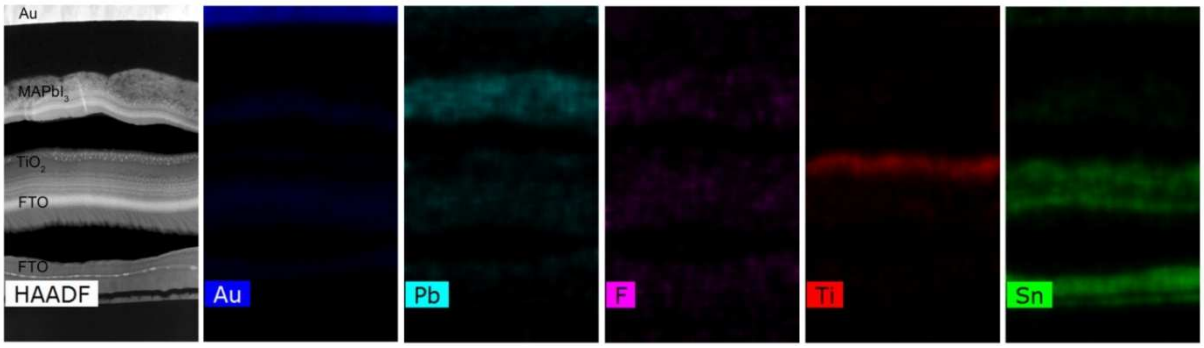

Figure S7 Cross-sectional HAADF image and EDS mapping of the $MAPbI_3$-PFA device, obtained from the FIB and the STEM mode.

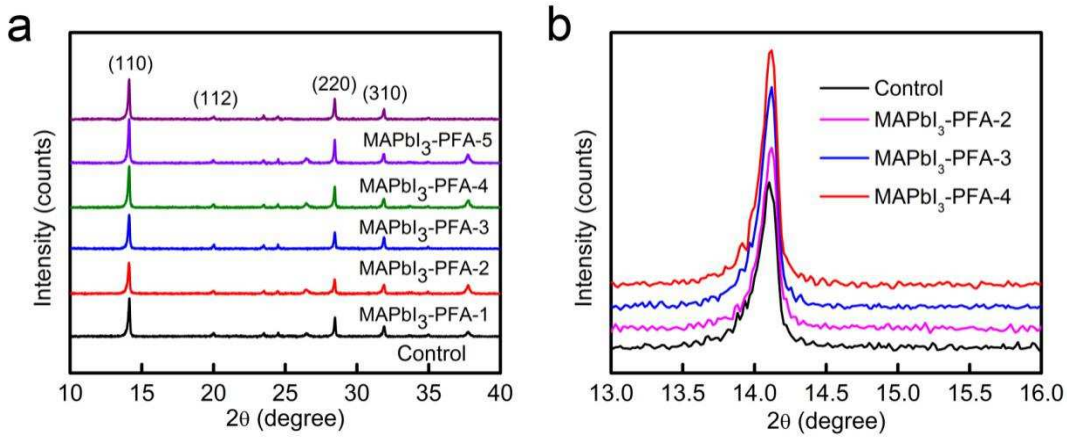

Figure S8 XRD patterns of co-passivated perovskite films with different concentrations: **(a)** 10-40°and **(b)** 13-16°

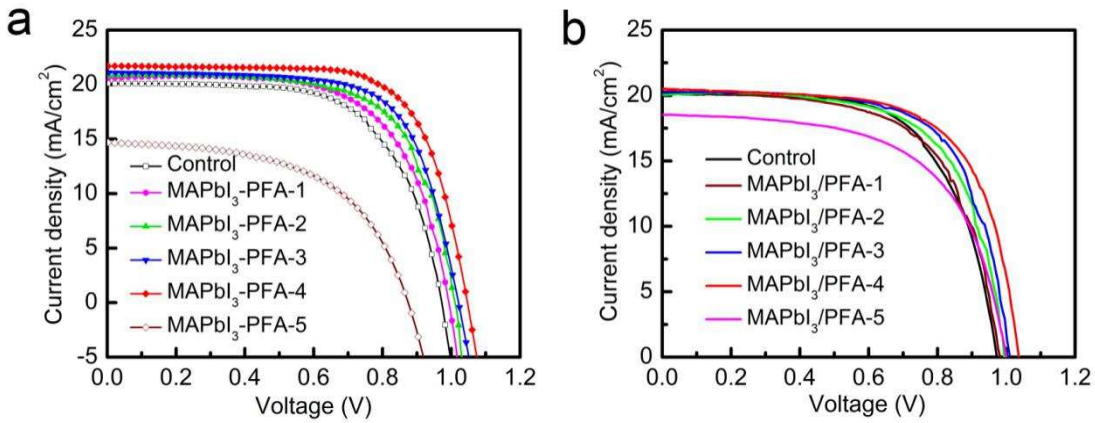

Figure S9 *J-V* curves of the champion PSCs for **(a)** $MAPbI_3$-PFA and **(b)** $MAPbI_3$/PFA with different concentrations.

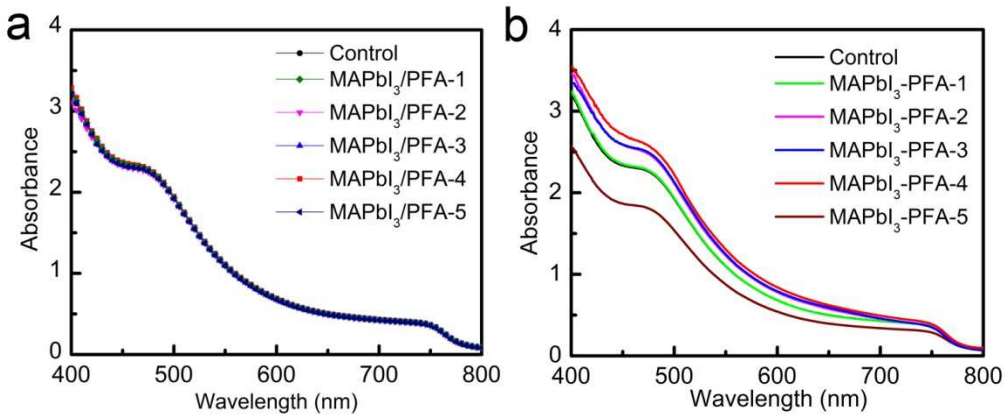

Figure S10 UV-Vis spectra of **(a)** $MAPbI_3$/PFA-4 films and **(b)** $MAPbI_3$-PFA films with different concentrations of PFA.

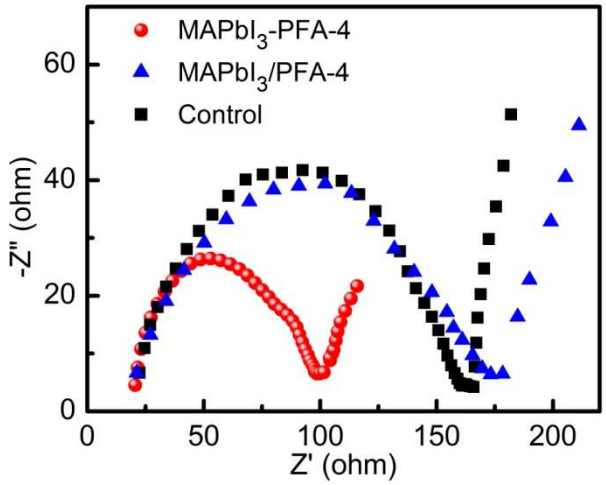

Figure S11 Nyquist plots of $MAPbI_3$, $MAPbI_3$/PFA-4 and $MAPbI_3$-PFA-4 devices measured at a bias of 0.8 V under simulated AM1.5 illumination.

The results from EIS reveal that the values of R_S are similar for these three devices, but the co-passivated device exhibits a much lower charge transfer resistance (95.2 Ω) than that of the control (1441.5) and surface-only passivated devices (149.7 Ω).

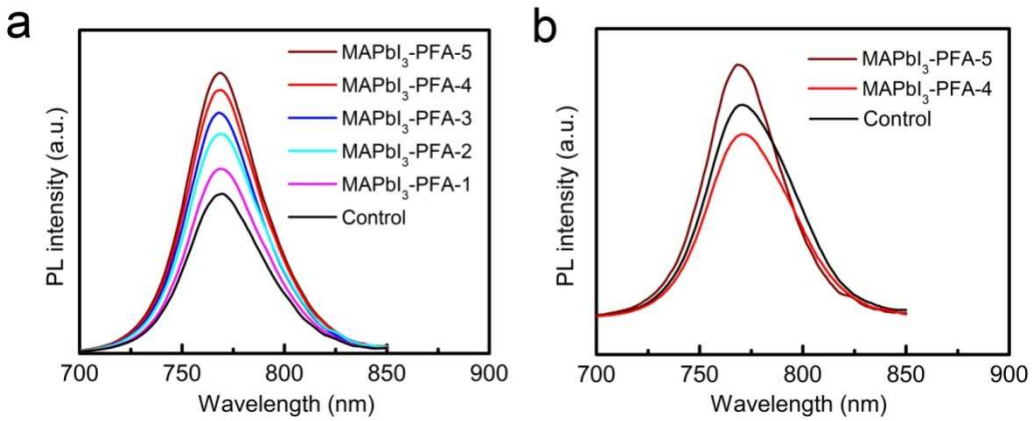

Figure S12 Steady-state PL spectra of **(a)** $MAPbI_3$-PFA and **(b)** $MAPbI_3$-PFA-HTL films with different concentrations of PFA.

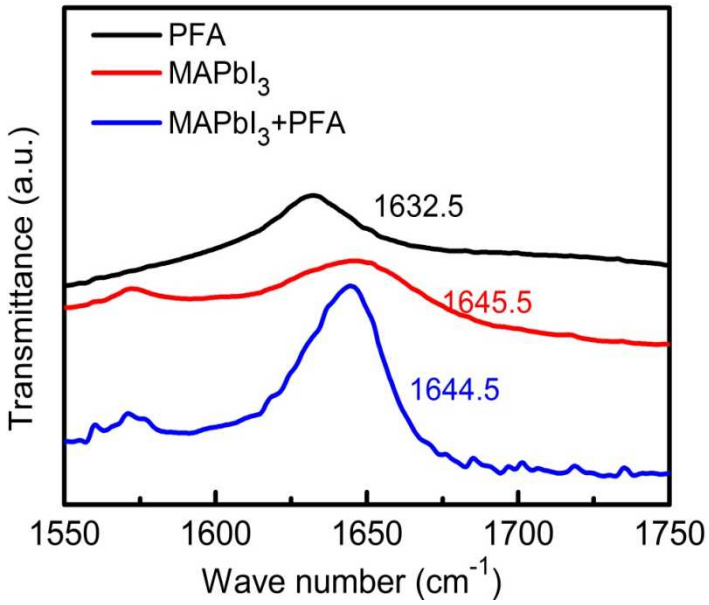

Figure S13 FTIR spectra of the PFA, $MAPbI_3$, and $MAPbI_3$+PFA films.

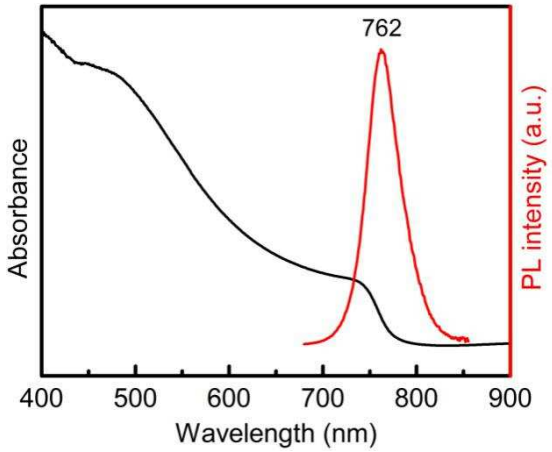

Figure S14 UV-Vis spectrum and steady-state PL spectrum of the CsFAMA film.

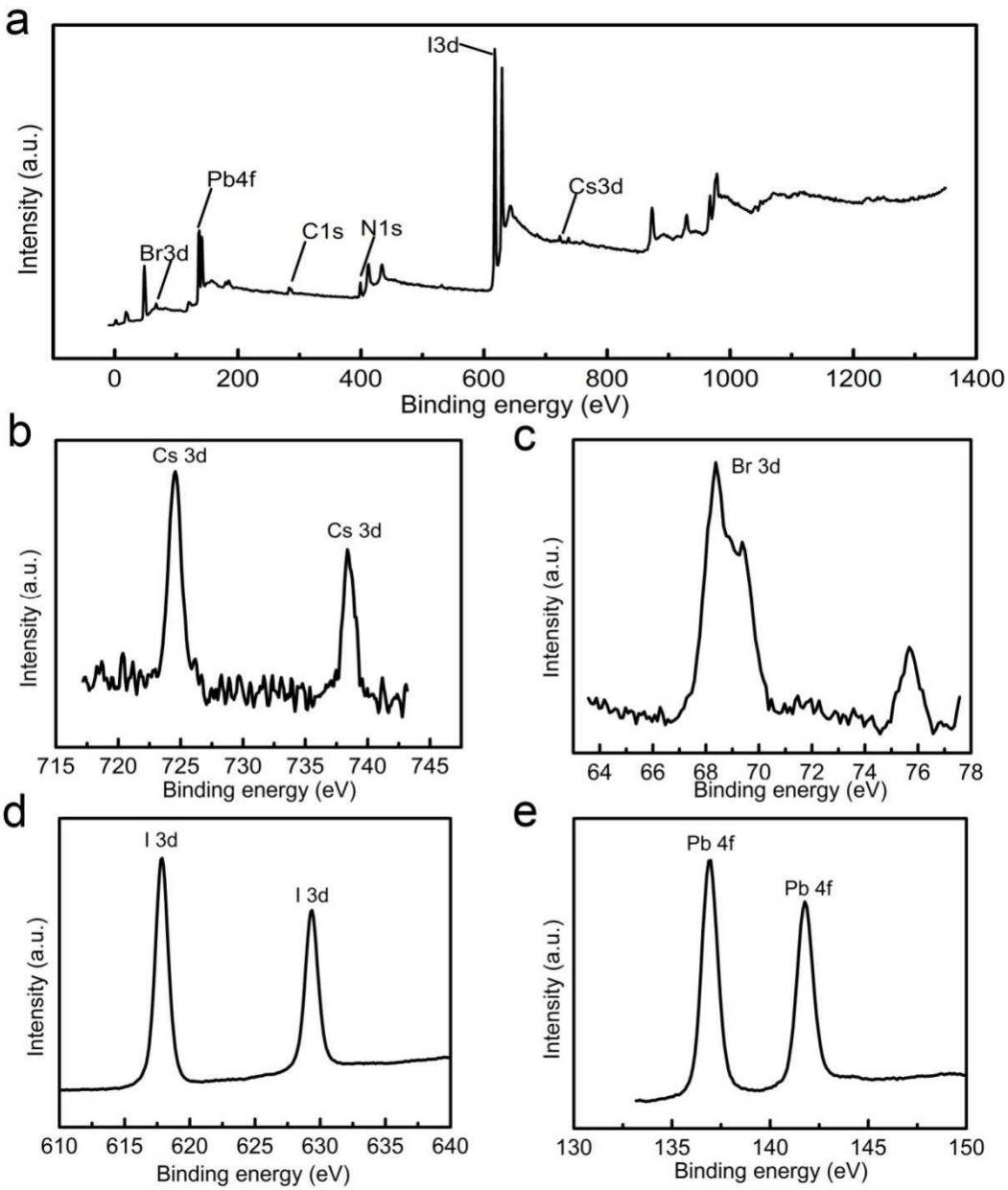

Figure S15 (a)XPS spectrum and binding energies of **(b)** Cs_{3d}, **(c)** Br_{3d}, **(d)** I_{3d}, and **(d)** Pb_{4f} of the CsFAMA-PFA film.

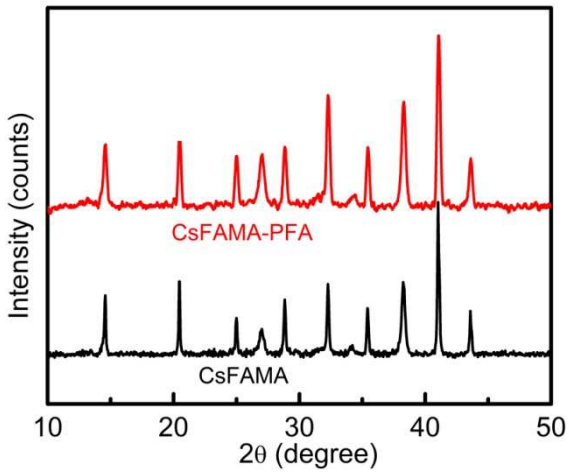

Figure S16 XRD patterns of the CsFAMA and CsFAMA-PFA films.

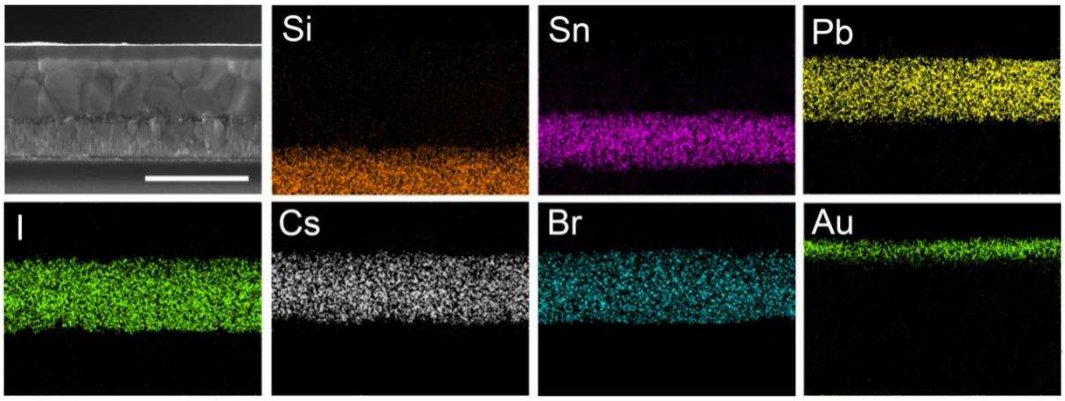

Figure S17 SEM-EDS mappings of Si, Sn, Pb, I, Cs, Br, and Au for a CsFAMA device. The scale bar is 1 μm.

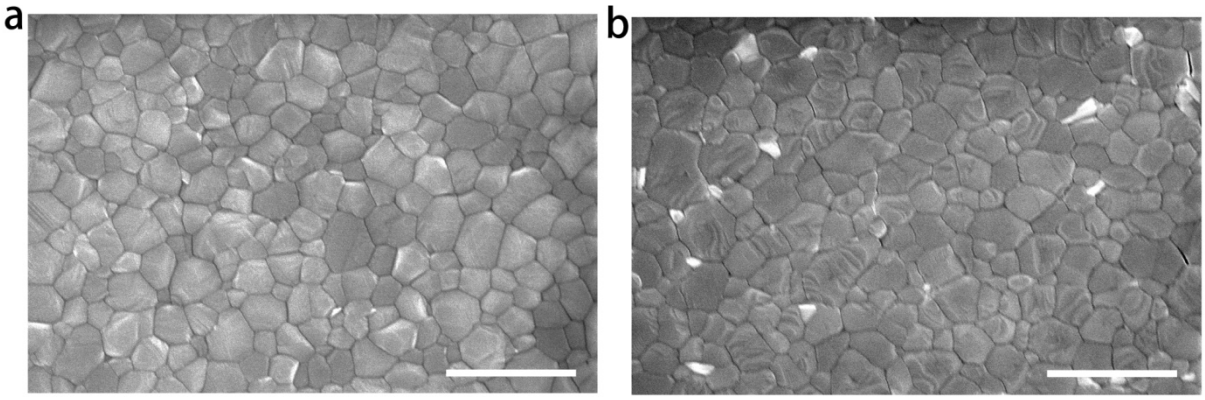

Figure S18 Surface morphologies of the CsFAMA (a) and the CsFAMA-PFA-4 (b) films.

The scale bar is 1 μm.

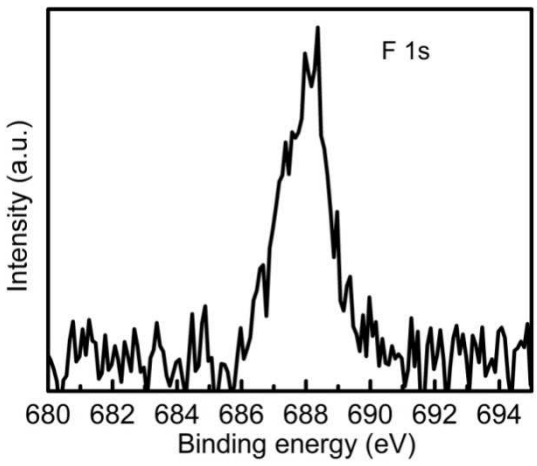

Figure S19 Binding energy of F_{1s} at the surface for the CsFAMA-PFA-4 film.

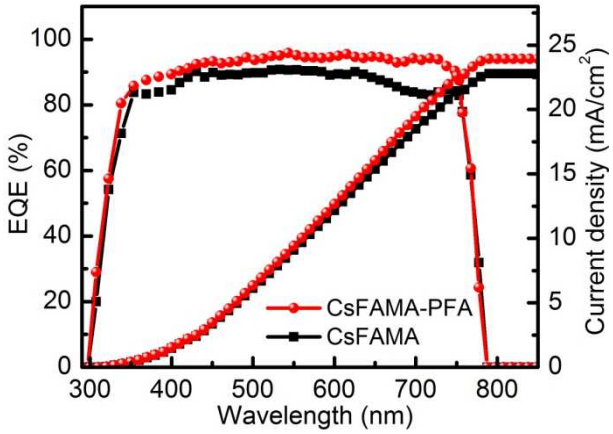

Figure S20 EQE spectra together with integrated J_{sc} for the CsFAMA-PFA and CsFAMA devices.

The EQE measurements indicate that co-passivation in CsFAMA based devices results in a broad plateaus with exceeding 90% along the whole absorption spectrum. The calculated integrated J_{sc} values are 22.77 and 23.93 mA/cm^2 for devices of CsFAMA, and co-passivation, respectively, which match well with the *J-V* measurements in **Figure 4g**.

Table S1 Summary of the best performance for the control, $MAPbI_3$-PFA-1, $MAPbI_3$-PFA-2, $MAPbI_3$-PFA-3, $MAPbI_3$-PFA-4, and $MAPbI_3$-PFA-5 cells. The scan rate is 0.2V/s.

Devices	Scan Direction	J_{sc} (mA cm^{-2})	V_{oc} (V)	FF (%)	Efficiency (%)
Control	Reverse	20.14	0.98	64.39	12.71
	Forward	20.14	0.95	45.37	8.68
$MAPbI_3$-PFA-1	Reverse	20.55	0.99	60.33	12.27
$MAPbI_3$-PFA-2	Reverse	20.92	1.01	67.08	14.17
$MAPbI_3$-PFA-3	Reverse	21.11	1.02	68.83	14.82
$MAPbI_3$-PFA-4	Reverse	21.71	1.05	70.97	16.18
	Forward	21.70	1.05	70.16	16.00
$MAPbI_3$-PFA-5	Reverse	14.84	0.87	54.45	7.01

Table S2 Summary of the best performance for the control, $MAPbI_3$/PFA-1, $MAPbI_3$/PFA-2, $MAPbI_3$/PFA-3, $MAPbI_3$/PFA-4, and $MAPbI_3$/PFA-5 cells. The scan rate is 0.2V/s.

Devices	Scan direction	J_{sc} (mA/cm^2)	V_{oc} (V)	FF (%)	Efficiency (%)
Control	Reverse	20.14	0.98	64.39	12.71
	Forward	20.14	0.95	45.37	8.68
$MAPbI_3$/PFA-1	Reverse	20.31	0.98	64.74	12.89
$MAPbI_3$/PFA-2	Reverse	20.23	0.99	65.72	13.16
$MAPbI_3$/PFA-3	Reverse	20.20	1.01	67.08	13.69
$MAPbI_3$/PFA-4	Reverse	20.45	1.04	68.10	14.48
	Forward	20.52	1.02	65.86	13.78
$MAPbI_3$/PFA-5	Reverse	18.50	1.00	60.18	11.12

Table S3 Fast PL lifetime (τ_1), slow PL lifetime (τ_2), and average lifetime (τ_{avg}) for the control, surface-only passivation, and co-passivation films.

Passivation Route	τ_1 (ns)	A_1 (%)	τ_2 (ns)	A_2 (%)	τ_{avg} (ns)
Co-passivation	23.7	26	121.2	74	95.85
Surface-only passivation	18.3	34	102.7	65	72.98
Control	2.9	54	17.8	46	9.75

Table S4 Photovoltaic parameters of perovskite devices before and after co-passivation.

Sample	Scan direction	J_{SC} (mA/cm^2)	V_{OC} (V)	FF (%)	Champion PCE (%)
Control	Forward	23.42	1.09	64.55	16.48
	Reverse	23.42	1.11	75.16	19.53
Co-passivation	Forward	24.06	1.13	78.26	21.28
	Reverse	24.10	1.14	77.56	21.31

Supporting References:

[1] Q. Dong, Y. Fang, Y. Shao, P. Mulligan, J. Qiu, L. Cao, J. Huang, *Science* **2015**, *347*, 967.